Poor remyelination of large lesions is attributable to failed oligodendrocyte progenitor cell recruitment.

James J. M. Cooper, BS[1], Jessie J. Polanco, PhD[2], Darpan Saraswat, PhD[1], Jennifer Peirick, DVM[3], Anna Seidl, Yi Li, Dan Ma, PhD[4], Fraser J. Sim, PhD[1,2]

Department of Pharmacology and Toxicology[1], Neuroscience Program[2], Lab Animal Facilities[3], Jacobs School of Medicine and Biomedical Sciences, University at Buffalo, Buffalo, NY.

Translational Medicine Research Group[4], Aston Medical School, Aston University, Birmingham, United Kingdom.

Address correspondence to:

Fraser Sim, Ph.D.
Department of Pharmacology and Toxicology
Jacobs School of Medicine and Biomedical Sciences
University at Buffalo
955 Main Street
Buffalo, NY 14203
716-829-2151
fjsim@buffalo.edu

Keywords: demyelination, remyelination, oligodendrocyte progenitor.

Running title: Poor Recruitment in Rabbit Model of Demyelination

Abstract, 250; Introduction, 827; Discussion, 2157; Tables: 0, Figures: 8

Acknowledgements: This work was supported by the Department of Defense Congressionally Directed Medical Research Programs (W81XWH-21-1-0387), NINDS grant (R01NS104021), National Multiple Sclerosis Society (RG-1701-26750), the Kalec Multiple Sclerosis Foundation, the Change MS Foundation. JJP received additional support from NIGMS (R25GM09545902), NCATS (UL1TR001412-S1), and New York State Department of Health (Empire State Stem Cell Fund) through the Stem Cells in Regenerative Medicine Fellowship (NYSTEM C30290GG). We

acknowledge support provided by the Center for Computational Research at the University at Buffalo for use of the academic compute cluster for training the Keras-based convolution network.

Conflict of Interest: The authors declare no competing financial interests.

Abstract

Objective:

The development of remyelination-inducing therapies for the treatment of multiple sclerosis (MS) has largely focused on driving oligodendrocyte differentiation. However, while rodent lesions display efficient remyelination and have a substantial oligodendrocyte progenitor cell (OPC) pool, the same is not true in MS lesions. Thus, we hypothesized that supernumerary densities of OPCs are required for efficient remyelination.

Methods:

We characterized oligodendroglia dynamics in a rabbit model of lysolecithin-induced persistent demyelination. To investigate volume dependance of these effects, we induced both large (10x mouse volume) and small (1x) lesions.

Results:

Following WM demyelination, the density of mature oligodendrocytes failed to return to normal levels for at least 6 months, consistent with chronic demyelination. Similar to MS, the density of recruited OPCs in the rabbit rarely exceeded that of normal appearing white matter. OPC activation was substantially delayed/prolonged relative to murine lesions, however only a small portion underwent proliferation. Instead, we observed upregulation of the OPC quiescence marker, Prrx1, in the lesion border. While small lesions displayed decreased OPC proliferation and marginally improved rates of oligodendrogenesis, OPC density was equivalent to large lesions.

Interpretation:

Inefficient oligodendrogenesis in the rabbit is accompanied by limited OPC recruitment which, in turn, appears to be limited by insufficient proliferation and pathological Prrx1 quiescence. Prolonged OPC activation may prevent oligodendrocyte differentiation and decouple remyelination from the attendant inflammatory response. As such, the rabbit model provides a valuable tool for understanding the mechanisms which limit progenitor recruitment and thereby contribute to the failure of remyelination in MS.

68 **INTRODUCTION**

69 Primary demyelination is most commonly associated with multiple sclerosis (MS), a disease
70 where half of patients will require walking assistance after a decade of disease (Confavreux et
71 al., 2000). Immune-mediated demyelination and loss of oligodendrocytes (OL) results in functional
72 neurologic deficit. In most experimental models, remyelination relies on restoration of the OL
73 population through first the recruitment (both migration and proliferation) of oligodendrocyte
74 precursor cells (OPCs) and then their subsequent differentiation and maturation into
75 oligodendrocytes (Franklin and Ffrench-Constant, 2017). OPCs are a multipotent stem cell
76 population that are distributed throughout the adult CNS. While the role of adult OPCs in normal
77 brain remains elusive, OPCs are responsible for the replacement of lost OLs in the context of
78 demyelination (Hughes et al., 2013, Zawadzka et al., 2010). Following a demyelinating event,
79 OPCs migrate into the damaged region from adjacent healthy tissue and begin to proliferate. The
80 expression of activation markers, such as Sox2, are downregulated as OPC differentiate into OLs
81 (Zhao et al., 2015). Newly generated OLs engage and ensheath denuded axons and upregulate
82 myelin proteins resulting in the production of a thin myelin sheath with shorter internodes that is
83 capable of restoring saltatory conduction (Lubetzki et al., 2020).

84 While remyelination is a common feature of early relapsing-remitting MS, remyelination
85 failure becomes more common with increasing disease duration and age (Franklin and Ffrench-
86 Constant, 2017). Remyelination failure is thought to be due to the malfunction of one or more
87 stages of oligodendrocyte regeneration: namely OPC recruitment, differentiation, and myelin
88 formation (Franklin and Ffrench-Constant, 2017). While quiescent OPCs are associated with
89 chronic demyelination in MS (Wolswijk, 1998), the prevailing theory in the field has been that
90 remyelination fails in MS due to a failure of differentiation. In response, a number of drug
91 candidates aimed at boosting endogenous remyelination through the promotion of OPC
92 differentiation have been developed and advanced to clinical trials after successful preclinical
93 results, notably opicinumab (anti-Lingo1) (Mi et al., 2005) and clemastine (Mei et al., 2014).
94 Unfortunately, while both were able to improve a functional test indicative of remyelination in the
95 optic nerve, neither was able to significantly impact clinical outcome or imaging endpoints in initial
96 trials (Green et al., 2017, Mellion et al., 2017, Cadavid et al., 2019). The paradoxical success of
97 differentiation-promoting therapies in rodent models, but little success in clinical trials, suggests
98 fundamental differences in the rate-limiting steps between remyelination in animal models and
99 human MS.

100 In small rodent models of demyelination, the density of OPCs quickly rises two-three fold
101 above that of normal white matter shortly following lesion formation (Sim et al., 2002, Ulrich et al.,

102 2008, Kucharova and Stallcup, 2015, Lin et al., 2006). In contrast, OPC density in MS lesion rarely
103 exceed that of normal appearing white matter (NAWM) (Lucchinetti et al., 1999, Kuhlmann et al.,
104 2008, Boyd et al., 2013, Moll et al., 2013, Tepavcevic et al., 2014). This is significant as small
105 rodent models, which remyelinate efficiently, have an extensive progenitor pool to draw upon.
106 Furthermore, there is little evidence that OPC recruitment is rate-limiting in the rodent (Franklin
107 and Goldman, 2015). Remyelination was not accelerated when the number of OPCs within the
108 lesion was experimentally increased (Woodruff et al., 2004) and only 1-3 rounds of division are
109 required to restore OPC density in rodent lesions (Foerster et al., 2020). Indeed, it is only after
110 long-term administration of cuprizone resulting in chronic depletion of OPCs that recruitment fails
111 and remyelination becomes inefficient (Mason et al., 2004). Thus, we hypothesized that
112 supernumery densities of OPCs are required for efficient remyelination.
113 In this study, we sought a model of inefficient remyelination to assess oligodendroglia
114 dynamics and one that more accurately recapitulates the burden of OPC recruitment seen in MS
115 lesions. To do this we utilized the rabbit lysolecithin model of demyelination which is characterized
116 by chronic demyelination for at least 6 months post-injection (Blakemore, 1978, Waxman et al.,
117 1979, Foster et al., 1980). We found that OPC recruitment was substantially inferior to
118 corresponding small rodent models and closely resembled the pattern observed in MS. Failed
119 recruitment was associated with a protracted period of OPC activation, an upregulation of
120 quiescence associated marker Prrx1 (Wang et al., 2018, Saraswat et al., 2021b), and an apparent
121 decoupling of OPC recruitment and differentiation with the innate immune response.
122 Fascinatingly, when smaller murine sized lesions were created in the rabbit, OPC recruitment was
123 similarly deficient resulting in delayed OL generation, indicating that delayed recruitment in the
124 rabbit is not entirely volume-dependent. While both small and large lesions show slower OL
125 repopulation relative to rodent lesions, small lesions repopulate more efficiently. Additionally,
126 large volume rabbit lesions exhibited distinct regional differences in the pattern of gliotic response,
127 OPC recruitment, activation and proliferation that evolved with time following induction of
128 demyelination. Together, we describe lysolecithin-induced lesions in the rabbit that recapitulate
129 several key features of demyelination in MS and which may more accurately predict the outcome
130 of novel remyelination-inducing therapies in clinical trials.
131

132 **MATERIALS AND METHODS**

133 *Animals and surgery*

134 All experiments were performed according to protocols approved by the University at Buffalo's
135 Institutional Animal Care and Use Committee. New Zealand White Rabbits were purchased as
136 needed (Female, average weight 2.96 ± 0.13 kg and average age 15.79 ± 0.53 weeks) (Charles
137 Rivers Laboratories, Wilmington, MA). Induction anesthesia was accomplished via intramuscular
138 injection of ketamine (35 mg/kg) and xylazine (5 mg/kg) into epaxial muscles. After loss of
139 consciousness, supplemental heating began and corneas were lubricated. The proximal 3 cm of
140 the tail was shaved to provide an optimal location for the pulse oximetry probe (far preferable to
141 use of ear or tongue). ECG leads and rectal temperature probe were placed. After pre-
142 oxygenation via face mask, rabbits were intubated in ventral recumbency with heads and necks
143 held in extension. A size 3.0 endotracheal tube was threaded over an 8-French urinary catheter.
144 After placement of the catheter through the glottis, the ET tube was advanced over the catheter
145 and into the trachea. Successful intubation was verified via immediate capnography. Upon
146 success, isoflurane was delivered via Bain Circuit (1-3%). An IV catheter was placed (marginal
147 ear vein), and the surgical site was shaved and prepped prior to moving the rabbit to the operating
148 room (OR). Pre-emptive, initial analgesics were administered (0.05 mg/kg buprenorphine,
149 subcutaneously (SC) and 1.5 mg/kg carprofen, SC).

150 Once moved onto the OR table, rabbits were immediately reconnected to isoflurane to
151 ensure a suitable anesthetic plane. Then, they were transiently disconnected from the Bain Circuit
152 to allow loose movement of the head into the stereotaxic frame (Kopf Model 902 Small Animal
153 Stereotaxic Instrument + Kopf Model 1240 Rabbit Adaptor + Rabbit Risers, Kopf Instruments,
154 Tujunga, CA). The endotracheal (ET) tube, was carefully moved to rest between the arms of the
155 Kopf Rabbit Adaptor. It was important that the ET tube was not advanced beyond 12 cm to avoid
156 bronchial obstruction. Once positioned, the capnograph and Bain Circuit were quickly
157 reconnected. At this time further careful positioning of the rabbit's head was possible via tooth
158 bar, zygoma clamps and nose clamp. General anesthesia could be maintained for the remainder
159 of the stereotaxic procedure with isoflurane. Spontaneous respirations were augmented by
160 manual intermittent positive pressure ventilations (IPPV). 0.1 mL bupivacaine (0.25%) or lidocaine
161 (2%, diluted 1:1 with 0.9% NaCl) was injected SC. A 7-8 cm incision was made alone the midline
162 of the scalp to expose both bregma (intersection of the sagittal and coronal sutures) and lambda
163 (intersection of the sagittal and lambdoid sutures). Both left and right arm Hamilton needles were
164 filled with distilled H_2O to prevent occlusion and ensure flow prior to lysolecithin loading. Placing
165 the needles point on either bregma or lambda, the dorsal-ventral (DV) relationship was adjusted

166 using the Kopf Rabbit Adaptor until bregma was 1.5 mm above lambda. The arms of the Kopf
167 frame were adjusted to a 20° angle, and the needle points were placed on bregma. The anterior-
168 posterior (AP), lateral-medial (LM), and DV of each arm was recorded. The following adjustments
169 were made to these values: AP= +0.5 mm, LM= +7.7 mm, DV= -5.7 mm. Injection sites were
170 confirmed previously via Evans Blue injection. Drill bits (Burrs for Micro Drill 19007-29, 2.9 mm,
171 Foster City, CA) were sterilized via dry micro bead bench side sterilizer for 1 minute and cooled
172 with room temp saline. In advance of drilling, topical articaine (4%) was dripped onto the skull and
173 allowed to absorb and dry over drilling skull sites. Drill holes were made through the skull to the
174 level of the meninges with constant saline stream to prevent parenchymal heat damage. A 30G
175 needle was then used to puncture the meninges to allow for free passage of the Hamilton needle.
176 1% lysolecithin was then injected at a rate 0.1 µl/min, with 5-minute wait times between microliters
177 to allow for diffusion. Once injection was completed, the needles were left in place for 20 additional
178 minutes to allow for diffusion. Either 5 µL (large volume lesion) or 0.35 µL (small volume lesion)
179 or lysolecithin was injected.
180 Post-operatively, buprenorphine was administered (0.05 mg/kg, SC) 4 hours after the
181 initial dose, and carprofen (1.5 mg/kg, SC) was continued twice daily for a total of 4 consecutive
182 days. Rabbits were monitored daily after surgery and assessed for: mentation, weight loss from
183 baseline, appetite, water consumption, amount and character of feces, amount of urination, and
184 presence of neurologic signs. Post-surgical weight loss peaked at 28 dpl, followed by a rapid
185 recovery (data available upon request).

186 *Tissue processing*

187 Animals were sacrificed at 7, 14, 21, 56, or 180 days post-lesion (dpl) by transcardial perfusion of
188 saline followed by 4% paraformaldehyde under deep anesthesia. Following decapitation, whole
189 brain tissue was extracted and post-fixed for 30 minutes in 4% paraformaldehyde. For
190 cryopreservation, the tissue was first left in 1x PBS overnight, then transferred into a 7.5% sucrose
191 solution overnight, and finally 15% sucrose overnight. Cryoprotected tissue was then frozen in
192 optimal cutting temperature medium (Tissue-Tek). Serial, 16 µm-thick coronal sections were cut
193 using a Leica cryostat, and stored in -80 °C freezer until processing.
194 To identify lesion location and volume, every 10th section was washed with 1x PBST (x3
195 by 5 min), stained with FloroMyelin for 1 hour at room temperature (1:300, Thermo Fisher
196 Scientific) and 4′,6-Diamidino-2-phenylindole dihydrochloride (DAPI) for 3 minutes (1:5000,
197 Sigma Aldrich), and mounted in prolong gold (Thermo Fisher Scientific). Lesions were identified
198 as regions with lesser FloroMyelin signal and corresponding hypercellularity by DAPI, compared

199 to surrounding white matter. Cross-sectional lesion areas were calculated for both left and right
200 hemisphere lesions using the NIH ImageJ software, and the largest cross-sectional area for each
201 lesion was identified as the lesion center.

202 *Estimation of lesion volume*

203 Lesion volume was calculated from the measured cross-sectional areas determined by
204 FloroMyelin staining using Cavalieri's estimator of morphometric volume (Rosen and Harry,
205 1990):
206

207 $$V_c = d\left(\sum_{i=0}^{n}(y_i)\right) - (t)y_{MAX}$$

208

209 Where V_c is the Cavalieri's estimated volume, d is the distance between sections, y_i is the cross-
210 sectional area of section i, t is the thickness of the sections, and y_{MAX} is the largest cross-
211 sectional area of the lesion. Since every 10th section was stained, d = 160 μm, and t = 16 μm.

212 *Immunohistochemistry (IHC)*

213 Slides immediately adjacent to the lesion centers, identified by FloroMyelin staining, were used
214 for all immunohistochemical procedures. In general sections were permeabilized for 1 hour with
215 1% Triton X-100 (Alfa Aesar) and 0.25% Tween 20 (Calbiochem). Sections were blocked for 1
216 hour with a solution containing 0.5% Triton X-100, 5% bovine serum albumin (BSA), and 5%
217 normal donkey serum. For cytoplasmic antigens such as CC1, sections were permeabilized with
218 a 0.1% saponin and 1% normal donkey serum for 15 min and blocked for 1 hr with a 5% donkey
219 serum and 0.05% saponin. Primary antibodies utilized were goat anti-Olig2 (1:100, R&D
220 Systems), mouse anti-CC1 (1:50, Millipore), mouse IgG2a anti-SOX2 (1:100, R&D Systems),
221 mouse IgG1 anti-Ki67 (1:25, Fisher Scientific), rat IgG2a anti-MBP (1:300, Abcam Inc.), goat IgG
222 Smi311 & Smi312 (1:1000, BioLegend), rabbit IgG anti-App (1:500, Thermo Fisher), rabbit IgG
223 anti-Iba1 (1:300, Wako Chemicals), and mouse IgG1 anti-Gfap (1:400, Sigma-Aldrich). Alexa 488,
224 594, and 647-conjugated secondary antibodies (Invitrogen) were used at 1:500. Lesion areas
225 were captured at 10X, 20X, and 60X magnification using an Olympus IX83 with IX3-SSU
226 motorized stage and image tiles stitched via cellSens software. Images of immunostained
227 sections were aligned with their corresponding FloroMyelin stained section to accurately mark
228 lesion boundaries, with exclusion of any portion of the lesion which extends into the gray matter.
229 Cells counts were determined via a semi-automated, machine learning assisted, counting process

230 (code available upon request). The Keras based convolution network was trained on a set of
231 ~3250 CC1 positive and ~3250 CC1 negative pre-classified images (supervised learning).

232 *Fluorescence in situ hybridization*

233 Fluorescence in situ hybridization was performed with probes targeting Prrx1 (GenBank
234 accession #NM_011127.2) mRNA by using the RNAscope Fluorescent Multiplex Detection Kit
235 (Advanced Cell Diagnostics) according to the manufacturer instructions and as described
236 previously (Wang et al., 2018, Saraswat et al., 2021a). Fixed sections were baked at 60°C for 30
237 min, washed with ethanol, followed by tissue pretreatment, and probe hybridization following
238 RNAscope fluorescence multiplex assay, and sections were counterstained with DAPI to visualize
239 nuclei. Positive signals were identified as punctate dots present in nucleus and cytoplasm.

240 *Statistics*

241 All statistical testing was completed using GraphPad Prism Version 8.4.0. The control
242 group for all analyses of cell numbers and phenotypes was normal white matter (NWM) from
243 uninjured animals, or normal appearing white matter (NAWM) from a region distant from the
244 lesion. Groups comprised either time-points following injection of lysolecithin, regional analysis
245 within the lesion, or small vs large volume lesions. For all reporting, an experimental unit
246 comprised a single lesion. A minimum of 4 experimental units (lesions) per group was set *a priori*
247 and along with a requirement for at least three animals per group. Criteria for lesion inclusion
248 were established *a priori*. Only lesions located within internal capsule white matter were included
249 in the analysis. No white matter lesions regardless of size were excluded from the analysis.
250 Rabbits were allocated to each group in a randomized fashion based on availability from the
251 vendor and surgical schedule. Manual cell count validations for all quantitative measures were
252 performed in a blinded fashion. Normality of data was tested in GraphPad using the D'Agostino-
253 Pearson omnibus test. For analysis of time-series data, one-way ANOVA with Tukey's post-hoc
254 testing was performed. For analysis of time-series and region delimited/volume delimited data,
255 two-way ANOVA with Sidak's post-hoc testing was performed. Only a portion of pairwise
256 comparisons were highlighted, however full pairwise statistical comparisons are available upon
257 request.

258 *Data availability*

259 The data that support the findings of this study are available upon reasonable request.

260

261 **RESULTS**

262 **Large lysolecithin-induced lesions in the rabbit persisted for at least 6 months.**

263 To test the hypothesis that supernumery densities of OPCs are required for efficient
264 remyelination, we sought to characterize OPC dynamics in a model of inefficient remyelination.
265 Lysolecithin-induced lesions in the sizable white matter tracts of the rabbit have been noted to
266 persist for at least 6 months (Blakemore, 1978, Foster et al., 1980, Waxman et al., 1979). To
267 induce demyelination, we stereotactically injected lysolecithin into the internal capsules of adult
268 New Zealand White rabbits (bilateral injections of 1% lysolecithin, 5 µl) (**Fig. 1A**). We first
269 examined lesion formation at 14 days post lesion (dpl). Overlay of a mouse coronal section
270 included for size reference. Similar to murine lesions, lysolecithin induced focal demyelination at
271 the site of injection and resulted in a clearly demarcated region of hypercellularity that precisely
272 matched the region of myelin loss (**Fig. 1B**, white dashed line). Volumetric analysis by serial
273 section reconstruction of the lesion indicated a comet-like appearance with a relatively spherical
274 region of demyelination corresponding to the site of injection and a tapered region extending in
275 the posterior-ventral direction, likely due to diffusion within the fascicles of the internal capsule.
276 The mean maximal cross-sectional area and volume peaked at 14 dpl (volume: 3.57 ± 0.3 mm^3,
277 area: 1.90 ± 0.2 mm^2, n = 8) (**Fig. 1C-D**). Following the peak in lesion area at 14 dpl, lesion area
278 gradually declined with time (21 vs 14 days, Tukey's p = 0.032). In stark contrast to rodent models,
279 large regions of demyelination persisted in the rabbit even at 180 dpl by which time rodent models
280 have typically resolved.

281 **Insufficient recruitment of OPCs in the rabbit was associated with prolonged suppression**
282 **of oligodendrocyte repopulation.**

283 We next sought to characterize OPC recruitment and differentiation following demyelination in the
284 rabbit brain (**Fig 2**). We assessed the recruitment and differentiation status of oligodendrocyte
285 lineage cells using Olig2 to label the entire oligodendrocyte lineage and CC1/Olig2 to label post-
286 mitotic oligodendrocytes (OL) (**Fig. 2A**). Following demyelination, $Olig2^+$ cell density was
287 significantly reduced more than three-fold at 7 dpl (Tukey's p < 0.0001) and, unlike small rodent
288 models, never exceeded that of normal white matter (NWM) thereafter (**Fig. 2B**). The density of
289 OPCs/immature oligodendrocytes, defined as $CC1^-Olig2^+$ cells, increased between 7 and 14 dpl
290 and remained stable at later time points (**Fig. 2C**). Similar to MS lesions, the density of OPCs
291 never significantly exceed that of NWM (**Fig. 2C**). Following lysolecithin injection, the lesion was
292 essentially devoid of mature OLs at 7 dpl (NWM = 877.8 ± 62 vs 7 dpl = 79.9 ± 14 cells/mm^2) (**Fig.
293 2D**). By 8 weeks, OL density had partially recovered and reached a plateau but remained nearly

294 half that of NWM at 8 weeks (NWM = 877.8 ± 62 vs 56 dpl = 453.9 ± 64.65 cells/mm^2, Tukey's p
295 < 0.0017). The proportion of CC1$^+$ oligodendrocytes amongst the Olig2$^+$ population has been
296 used to infer the rate of oligodendrocyte differentiation. Intriguingly, while the proportion of mature
297 OLs increased with time until 21 dpl (**Fig. 2E**), the proportion of oligodendrocytes did not increase
298 at later time points suggesting that on-going oligodendrocyte generation may not continue after
299 this initial period. The distribution of OPCs to OLs remained aberrant at 6-months indicating a
300 chronic change in oligodendrocyte lineage homeostasis (NWM = 66.3 ± 3.2% vs 180 dpl = 42.2
301 ± 9.1%). Together, these data suggest that OPC recruitment in the rabbit occurring following
302 demyelination is insufficient to generate sufficient oligodendrocytes necessary to repair these
303 lesions. The relative failure of OPC recruitment contrasted with small rodent models while
304 resembling that of MS lesions.

305 **OPC activation and proliferation were impaired following demyelination in the rabbit**

306 Insufficient oligodendrocyte progenitor cell (OPC) recruitment in the rabbit may result from a
307 failure of parenchymal OPCs to respond appropriately to environmental signals associated with
308 demyelination. As such, we next sought to assess OPC activation and proliferation. The
309 transcription factor Sox2 is upregulated in activated adult OPCs following demyelination and is
310 necessary for OPC recruitment and successful remyelination (Zhao et al., 2015). As expected, in
311 normal rabbit white matter the majority of Olig2$^+$ cells were Sox2$^-$ and Ki67$^-$ (**Fig. 3A**). Following
312 demyelination, recruited OPCs progressively upregulated Sox2, such that the majority of Olig2$^+$
313 cells in the lesion area coexpressed Sox2 by 14 dpl (NWM = 3.2 ± 2%, 14 dpl = 51.4 ± 3%) (**Fig.
314 3B**). Overall, the density of Sox2$^+$Olig2$^+$ OPC peaked at 14 dpl (NWM vs 14 dpl, 14 dpl vs 180
315 dpl, Tukey's p < 0.0001 and p < 0.0001, respectively), and returned to control levels by 6 months
316 (NWM vs 180 dpl, Tukey's p > 0.05) (**Fig. 3B-E**). The pattern of Sox2$^+$ expression among OL
317 lineage cells largely corresponded with their proliferative capacity defined by Ki67 expression.
318 The proportion of Ki67$^+$ cells peaked at 14 dpl and returned to baseline by 6 months (NWM vs 14
319 dpl, 14 dpl vs 180 dpl, Tukey's p = 0.004 and p = 0.02, respectively) (**Fig 3B-D, F**). However,
320 unlike mouse these responses were substantially smaller in magnitude and delayed relative to
321 lesion induction. For example, mouse Sox2$^+$ OPCs were highly proliferative at 5 dpl with 50%
322 Ki67$^+$ (Zhao et al., 2015). In contrast, rabbit Sox2$^+$ OPC proliferation did not peak until 56 dpl and
323 never exceeded 30% (NWM vs 56 dpl, Tukey's p = 0.025) (**Fig. 3G**). This indicates a far more
324 protracted period of OPC recruitment that ultimately fails to result in supernumerary OPC
325 generation.
326

327 **Microglial/macrophage response correlates with the pattern of OPC recruitment**
328 Next, we examined the microglial and astrocyte response following demyelination to determine
329 whether the failure to recruit supernumerary OPCs could be attribute to the pattern of the innate
330 immune response. In this regard, we noted substantial upregulation of Sox2 among Olig2
331 negative cells following demyelination (**Fig. 3B-D**). We confirmed that these Sox2^{+} cells were
332 largely reactive Gfap^{+} astrocytes that were concentrated within the center of the demyelinated
333 lesion (**Fig. 3H**). A substantial number of Sox2^{+}Olig2^{-} cells were observed within the lesion at all
334 time points, with statistically greatest numbers at 8 weeks followed by a reduction at 6 months
335 (NWM vs 56 dpl, 56 dpl vs 180 dpl, Tukey's p = 0.045 and p = 0.018, respectively) (**Fig. 3I**).
336 At 7 dpl, both microglial (Iba1) and astrocyte (Gfap) markers were upregulated throughout
337 the demyelinated lesion with a relatively homogenous pattern throughout the lesion area (**Fig.**
338 **4A**). At higher magnification, Iba1^{+} microglial largely adopted an ameboid morphology while
339 astrocytes were hypertrophic and reactive in appearance (**Fig. 4A**, insets). Interestingly, within
340 the lesion core ameboid microglia/macrophages commonly formed vesicular structures that were
341 surrounded by Gfap^{+} astrocytic processes (**Fig. 4I-K**). At later timepoints both
342 microglia/macrophage and astrocyte signals were more concentrated toward the lesion center
343 (**Fig. 4B-D**). While Gfap immunoreactivity remained elevated for 6 months, Iba1 was more
344 transient with a peak between 7-14 days. Consistent with this qualitative assessment, Iba1 mean
345 florescent intensity (MFI) peaked at 7 and 14 days and was significantly elevated relative to
346 normal appearing white matter (**Fig. 4E**) (NAWM; defined as matched uninjured corpus callosum
347 from the same cohort of animals, n=29). Iba1 remained elevated versus NAWM at each time point
348 including 56 dpl (NAWM vs 56 dpl, Tukey's p = 0.006). In contrast, the astrocytic response defined
349 by Gfap area remained significantly elevated throughout the experimental time course, with
350 significantly Gfap upregulation still apparent at 180 dpl (NAWM vs 180 dpl, Tukey's p = 0.02) (**Fig.**
351 **4F**). Unlike mouse spinal cord lysolecithin and experimental autoimmune encephalomyelitis
352 models (Dorrier et al., 2021), we did not observe substantial numbers of collagen 1-expressing
353 (Col1) fibroblasts within rabbit lesions at any time point. Together, these results suggest that
354 astroglial and microglial responses are distinct from one another in this model and intriguingly that
355 the overall microglial rather than the astroglial response corresponded to the pattern of OPC
356 activation and proliferation.

357 **Rabbit lesions exhibit region specific gradients of OPC activation and OL differentiation.**
358 While regional differences in MS lesions have been widely reported (Boyd et al., 2013, Absinta et
359 al., 2021), region-specific differences in murine models are difficult to assess due to their small

360 size. The larger rabbit lesions allowed us to better investigate region-specific lesion differences in
361 lesion evolution and correlate OPC recruitment with local gliotic responses. Surrounding the
362 central area of demyelination (**Fig. 5A,** white dashed line), we observed a defined region of mild
363 hypercellularity and disturbed myelin (Mbp) structure which we termed perilesion white matter
364 (PLWM) (**Fig. 5A**, blue dashed line) (**Fig. 5B-C**). The mean maximal cross-sectional area of the
365 PLWM expanded following lesion induction (**Fig. 5D**). Within the lesion, Mbp staining showed
366 abundant myelin debris at 7 dpl, with substantial clearance by 14 dpl (**Fig. 5E, 5G**). At 56 dpl,
367 there was a partial recovery of Mbp immunoreactivity in the PLWM, but it lacked the structure
368 observed in normal WM (**Fig. 5E, 5G**). Interestingly, PLWM exhibited increased numbers of both
369 microglia/macrophages and astrocytes at 21 dpl that generally resolved by 180 dpl (**Fig. 4G-H**).
370 Indicative of primary demyelination neurofilament (NF)-labelled axons were preserved at all time
371 points throughout the lesion (**Fig. 5F, 5H**). However, we noted a gradient of axonal density with
372 greater numbers of axons at the lesion edge (**Fig. 5F, 5H**). Consistent with the loss of axons in
373 the lesion core, we observed accumulation of App immunoreactivity specifically at 7 dpl which
374 disappeared at later time points (**Fig. 5F, 5H**). The lesion core was also enriched for microglial
375 and astrocytic antigens suggesting a more inflammatory core (**Fig. 4**). Thus, the rabbit lesion
376 displayed three distinct regions (PLWM, lesion edge, and lesion core) within which OPCs were
377 recruited and would have an axon substrate available for remyelination.

378 Next, we examined the pattern of OPC recruitment and differentiation in these regions
379 (**Fig. 6A-E**). As observed with flouromyelin staining, the PLWM, showed a clear alteration in
380 solochrome cyanine staining relative to NAWM (**Fig. 6A**). This corresponded with a reduction in
381 mature OL density ($CC1^+Olig2^+$). Across time points, the reduction in OL density corresponded to
382 lesion location, whereby mature OL density exhibited a gradient with the greatest density in the
383 PLWM (**Fig. 6B, Fig. 6F**) (Two-way ANOVA, region effect $p = 0.0001$). Consistent with a failure
384 to repair regardless of region, the density of mature OLs in the PVLM remained depressed relative
385 to NWM (unpaired t test, two-tailed, $p = 0.0001$). In MS lesions, OPCs tend to accumulate around
386 lesion borders (Heß et al., 2020). In contrast, the rabbit lysolecithin lesion showed the opposite
387 trend with the lesion core exhibiting the greatest $Olig2^+CC1^-$ defined OPC density at each time
388 point (Two-way ANOVA, region effect $p = 0.0017$), (**Fig. 6G**). Together, the regional analysis
389 confirmed the overall failure of OPC recruitment throughout the lesion with greatest recruitment
390 occurring in the lesion core. The relative lack of OPCs within the lesion edge suggesting a specific
391 failure of OPC activation and proliferation. We examined the proportion of $Sox2^+$ activated $Olig2^+$
392 cells in each region and observed that the $Sox2^+$ OPC accumulated in the lesion core (Two-way
393 ANOVA, region effect $p < 0.0001$) (**Fig. 6C, Fig. 6H**). This regional difference was inversely

394 related to mature OL density in consistent with previous observations that Sox2 can prevent OL
395 differentiation in mouse OPCs (Zhao et al., 2015).

396 **Pathological OPC quiescence may contribute to failed differentiation in the lesion edge**
397 We next sought to identify the potential mechanisms that may cause OPC recruitment to fail in
398 and around the rabbit lesion. We have previously shown that human OPCs expressing the
399 transcription factor Prrx1 enter a reversible state of quiescence that prevents their cell-cycle entry
400 and limits their capacity to myelinate host shiverer axons (Wang et al., 2018). Furthermore, Prrx1
401 mRNA is upregulated by inflammatory cytokines such as IFN-γ and found among non-cycling
402 OPCs within mouse lysolecithin lesions and human MS plaques (Wang et al., 2018). In rabbit
403 NAWM, we noted Prrx1-expression among many Olig2$^+$ cells (**Fig. 6I**). Similar to previous reports,
404 following induction of demyelination Prrx1 expression was found in both Olig2$^+$ oligodendrocyte
405 lineage and other Olig2$^-$ cells. However, unlike mouse lesions, we noted a striking accumulation
406 of Prrx1 expressing Olig2$^+$ cells in the lesion edge at 14 dpl (**Fig. 6J**). This was a transient
407 phenomenon as the overall level and number of Prrx1$^+$ cells decreased substantially by 56 dpl
408 (**Fig. 6K**). The accumulation of Prrx1$^+$Olig2$^+$ at the lesion edge suggests that OPCs entering the
409 demyelinating lesion rapidly upregulated Prrx1 and likely become quiescent, thereby reducing
410 their capacity to sufficiently repopulate the demyelination region.
411 In addition to Prrx1, we also noted an intriguing pattern of Olig2 immunoreactivity in a
412 subset of cells within the rabbit lesion. Unlike mouse lysolecithin lesions, a common though rare
413 observation was the presence of Olig2-expression within the cytoplasm of individual cells (**Fig.
414 6L**). The appearance of cytoplasmic Olig2 has been previously attributed to cells transitioning to
415 an astroglial fate via IFN-γ (Cassiani-Ingoni et al., 2006). Together these observations further
416 suggest that the microenvironment of the demyelinated rabbit brain was significantly different from
417 that of the adult mouse.

418 **Small volume lesions exhibited similar astrogliosis but relatively reduced
419 microglial/macrophage responsiveness.**
420 As large volume rabbit lesions require the generation of substantially more cells than mouse
421 models, we asked whether the deficits in OPC recruitment and differentiation could be attributed
422 to lesion volume alone. We created small volume lesions via injection of 0.35 μL lysolecithin.
423 Small volume lesions were 7-fold smaller by volume than large volume rabbit lesions, and closely
424 resembled the volume of murine lesions (Kucharova et al., 2011) (murine lesions = 0.4 mm^3, small
425 volume rabbit = 0.39 ± 0.1 mm^3, large volume rabbit = 3.6 ± 0.3 mm^3) (n=4 and 8, respectively).
426 Similar to large rabbit lesions, following demyelination small volume lesions displayed equivalent

427 levels of hypercellularity and astrogliosis (Gfap) compared to large volume lesions (**Fig 7A-B, 7D-**
428 **E**). Indeed, there were no significant differences between small and large volume lesions at any
429 time point (**Fig. 7H-I**). Intriguingly, we noted that small volume lesions had less intense Iba1
430 staining compared to large lesions (**Fig. 7C,F**) (Two-way ANOVA, volume main effect $p < 0.0001$).
431 Mean Iba1 intensity was highly significantly decreased relative to large volume lesions at both 7
432 and 14 dpl (Šídák's $p = 0.0015$ and 0.013, respectively) (**Fig. 7J**).

433 **OPC activation and proliferation in small lesions**

434 To determine whether OPC recruitment was altered in small volume lesions, we
435 interrogated activation and proliferation of OPCs using Sox2 and Ki67, respectively (**Fig. 8**). The
436 overall density of Olig2$^+$ cells following demyelination was similar between large and small lesions
437 (**Fig. 8A, E**). Unlike equivalently sized mouse lesions, Olig2 density never exceeded the control
438 level (dotted line). Two-way ANOVA revealed a statistically significant effect of lesion size on
439 Olig2 density ($F(1,22)=7.3$, $p = 0.013$) with the greatest relative increase in small lesions occurring
440 at 7 dpl.

441 Examination of Sox2 and Ki67 revealed far more apparent volume-dependent effects (**Fig.**
442 **8B-C**). The extent of Sox2 activation was significantly lower in small lesions with a >2-fold
443 decrease in Sox2$^+$Olig2$^+$ cell density at 14 dpl (Šídák's $p = 0.0015$) (**Fig. 8F**). This corresponded
444 with a profound reduction in the proportion of actively proliferating Ki67$^+$ OPCs (Two-way ANOVA,
445 volume; $F(2,21) = 19.68$, $p = 0.0002$) (**Fig. 8G**). As Olig2 expression is maintained in mature OLs,
446 we next examined the fraction of Ki67$^+$ cells among Sox2$^+$Olig2$^+$ activated OPCs (**Fig. 8H**). Very
447 few, <1%, of these OPCs expressed Ki67 suggesting that OPC proliferation is high dependent on
448 lesion volume in the rabbit and suggests that recruitment in small rabbit lesions is principally due
449 to migration from NAWM. This was in striking contrast with the proportion of Ki67$^+$ cells in
450 equivalently sized mouse lesions with 26.4 $\pm$ 1.4% and 7.5 $\pm$ 1.1% at 5 and 14 dpl, respectively
451 (Ki67% among Sox10$^+$ cells, n= 3-4 mice).

452 Although proliferation was substantially lower in small volume lesions, there was
453 surprisingly no significant difference in the density of CC1$^-$Olig2$^+$ OPCs between small and large
454 volume lesions (**Fig. 8I**). This likely reflects the reduced requirement for OPC generation. Large
455 lesions with 7-fold greater volume requires approximately 2-3 more cell divisions to achieve the
456 same density of OPCs. Interestingly, while the density of OPCs was equivalent at each stage, the
457 generation of CC1$^+$ mature OLs was significantly greater in small lesions (CC1$^+$Olig2$^+$ cell density;
458 Two-way ANOVA, volume main effect $p = 0.0035$) (**Fig. 8D, 8J**). In fact, small lesions were able
459 to successfully repopulate the lesion area with mature OLs (One-way ANOVA, $p = 0.017$). At 21

460 dpl, the density of mature OL was no longer significantly reduced compared to NWM (Tukey's p
461 = 0.30). The rate of oligodendrocyte generation was also significantly more rapid in small lesions
462 (**Fig. 8K**). By 7 dpl there was an increased proportion of mature OLs in small lesion relative to
463 large lesions (Šídák's, p = 0.019) (**Fig. 8K**). As such, the nature of OPC recruitment, being
464 principally migratory in small lesions and proliferative in large lesions, was associated with
465 differing rates of oligodendrogenesis. These results suggest that recruitment and differentiation
466 following demyelination exhibit both species- and volume-dependent influences that contribute to
467 a failure to coordinate OPC recruitment with differentiation and together lead to chronic
468 demyelination.

469 **DISCUSSION**

470 The optimal therapeutic strategy toward the goal of myelin restoration and thereby overcome the
471 inhibitory microenvironment present in chronic MS lesions remains elusive. Recent drug
472 candidates developed on the basis of promising results in various mouse models of demyelination
473 have not yet been successfully translated into a meaningful clinical therapeutic (Cadavid et al.,
474 2017, Cadavid et al., 2019, Green et al., 2017). This may be due, in part, to the already highly
475 efficient nature of remyelination in the mouse CNS and critical differences in human cell biology
476 (Dietz et al., 2016). Here, we show that inefficient remyelination occurs in the rabbit brain and
477 that, unlike mouse models, the oligodendrocyte progenitor cell (OPC) is largely unable to rapidly
478 repopulate the demyelinated lesion leading to MS-like chronic demyelination. Following
479 lysolecithin injection, rabbit lesions exhibited chronic gliosis and demyelination with preservation
480 of axons for at least six months. Notably, we found region-specific differences in the response of
481 OPCs to demyelination, with chronic activation of OPCs in the core associated with regions of
482 gliosis and increased oligodendrocyte (OL) generation in the lesion edge, a pattern commonly
483 found in MS (Heß et al., 2020). Fascinatingly, we found that the delayed and insufficient OPC
484 recruitment observed in rabbit lesions was not volume-dependent but likely due to species-
485 specific differences that include a greater predisposition to upregulate a marker of quiescence in
486 rabbit OPCs. Volume-specific differences did manifest as profound differences in the mechanism
487 of OPC repopulation, with migration or proliferation predominant in small and large lesions
488 respectively. These data support the need for additional models to investigate mechanisms
489 underlying chronic demyelination and highlight the species-specific differences that contribute to
490 remyelination failure.

491 Unlike several other experimental species including mouse, rat and cat, the rabbit
492 lysolecithin model of demyelination exhibits chronic demyelination, persisting at least 3-6 months
493 following injection of lysolecithin (Blakemore, 1978, Foster et al., 1980). This is similarly reflected
494 by poor remyelination in the rabbit following induction of EAE (Williams et al., 1982, Prineas et
495 al., 1969). In this study, we confirmed the presence of chronic demyelination in the rabbit brain
496 with preservation of axons and overt myelin loss remaining at 6 months. Although reported over
497 40 years ago, the mechanisms underlying the failure of rabbit remyelination have not been
498 investigated. Remyelination failure could result from a failure of surviving and/or newly-generated
499 OL within the lesion microenvironment to synthesize myelin sheathes or insufficient *de novo* OL
500 generation from resident progenitors (Franklin et al., 2021). While the current study is unable to
501 address the ability of surviving rabbit OLs to remyelinate axons, the studies by Waxman and
502 Blakemore do establish the potential for oligodendrocyte based remyelination as thinly

503 remyelinated axons are found within chronically demyelinated rabbit brain and spinal cord
504 (Blakemore, 1978, Foster et al., 1980). Our detailed study of OPC and OL cell dynamics at several
505 time points establish several distinguishing features of the rabbit model that may underly the
506 failure of remyelination. Unlike lysolecithin lesions in the mouse which result in increased OL
507 density relative to unlesioned white matter (Fancy et al., 2009), the density of OL in the rabbit
508 lesions never returns to normal levels and remains poorly repopulated with OLs at up to 6 months
509 following demyelination.

510 The failure to generate sufficient OLs in the adult rabbit may be caused by either a failure
511 to differentiate or an insufficient pool of OPCs able to undergo differentiation. Parenchymal adult
512 OPCs retain the capacity to generate new oligodendrocytes and are largely considered to be the
513 primary source of newly generated OLs following demyelination in the adult CNS (Serwanski et
514 al., 2018, Zawadzka et al., 2010). Differentiation occurs in a highly regulated manner and can be
515 influenced by a number of developmental and pathological processes (Fancy et al., 2011).
516 Likewise, the processes underlying OPC recruitment involve a combination of complex signaling
517 events that are activated by the local tissue microenvironment and inflammatory processes.
518 Together these lead to OPC migration and proliferation that are necessary for the appropriate
519 recolonization of demyelinated lesions, a process known as recruitment. In mouse models of
520 toxin-induced demyelination and EAE, OPC recruitment is not typically rate limiting (Franklin and
521 Goldman, 2015). Furthermore, approaches to improve recruitment have not meaningfully altered
522 the rate of myelin regeneration in focal mouse lesions. For example, overexpression of PDGF-AA
523 drives enhanced OPC recruitment following demyelination and yet this had no discernable effect
524 on the rate of remyelination (Woodruff et al., 2004). The progenitor pool in small rodents models
525 is especially capable of efficient recruitment and occurs following systemic depletion either by X-
526 irradiation (Chari and Blakemore, 2002) or pharmacogenetic depletion (Xing et al., 2021) and,
527 importantly, after demyelination. Repeated focal demyelination is not sufficient to deplete the
528 progenitor pool (Penderis et al., 2003) and only sustained depletion of OL lineage cells using 12-
529 week treatment can prevent efficient remyelination in the cuprizone model (Mason et al., 2004).
530 The relative success of OPC recruitment in the mouse is exemplified by the rapid regeneration of
531 OPC densities, 2-3 fold greater in demyelinated tissues than normal white matter (Sim et al.,
532 2002, Ulrich et al., 2008, Kucharova and Stallcup, 2015, Lin et al., 2006).

533 In contrast, rabbit lesions regardless of size are characterized by a failure of OPC
534 recruitment such that the density of OPCs never exceeds that of normal tissue and the
535 characteristic over-population of OPCs that occurs in the mouse and rat is absent. The rate of
536 recruitment is also comparatively delayed, reaching peak density only after 14 days. Whereas

537 mouse and rats reach peak progenitor density within the first week (Sim et al., 2002, Fancy et al.,
538 2004). While the dynamics of OPC recruitment in human are difficult to ascertain from postmortem
539 tissue, MS lesions similarly rarely display supernumerary OPC density (Lucchinetti et al., 1999,
540 Kuhlmann et al., 2008, Boyd et al., 2013, Moll et al., 2013, Tepavcevic et al., 2014). While our
541 data identify a substantial deficit in the ability of rabbit OPCs to repopulate regions of
542 demyelination, we also noted a relative failure in the ability of OPCs to undergo differentiation.
543 We observed a substantial decrease in the proportion of $CC1^+$ OL among the entire $Olig2^+$ lineage
544 relative to mouse/rat model systems. While this may represent a difference in the inherent rates
545 of OL difference in rabbit, an alternative hypothesis is that the failure of recruitment contributes to
546 failed differentiation. *In vitro* OL differentiation is dependent on the density of OPCs (Rosenberg
547 et al., 2008) and, similarly, following transplantation human OL differentiation is correlated with
548 the local density of human OPCs (Dietz et al., 2016). This suggests that below a certain threshold
549 local density of OPCs, the process of OL differentiation itself may be limited. Consist with this
550 hypothesis, remyelinated lesions and active lesions in MS, which have a higher propensity for
551 remyelination, tend to have higher densities of OPCs then chronic demyelinated lesions (Boyd et
552 al., 2013). Our data therefore are consistent with the model that critical species differences exist
553 in the capacity for OPCs to respond to demyelinating signals and that failed recruitment is the
554 primary determinant of failed remyelination in the rabbit model.

555 We next examined why OPC recruitment may be inadequate in the rabbit CNS.
556 Parenchymal OPCs are recruited from neighboring tissues and form an outside-in gradient of
557 OPC densities when depleted by X-ray irradiation (Chari and Blakemore, 2002). Intriguingly, we
558 consistently observed significantly higher densities of OPCs in the lesion core versus both lesion
559 edge and perilesion white matter. This suggests that the environment of the rabbit lesion may
560 differ in the signals capable of attracting and retaining OPCs within the lesion core (Boyd et al.,
561 2013, Piaton et al., 2011, Kerstetter et al., 2009).

562 Several pieces of evidence in our study point toward the importance of species difference
563 in the inadequacy of OPC recruitment in the rabbit. Sox2 is upregulated by the majority of OPCs
564 following demyelination in the mouse brain and is necessary for precursor proliferation such that
565 conditional deletion of Sox2 in OPCs leads to failed recruitment and remyelination (Zhao et al.,
566 2015). In the rabbit, Sox2 expression was substantially lower, occurring in far fewer OPCs and
567 over a much-protracted time course. This corresponded to a substantial relative reduction in the
568 rate proliferation with the peak occurring at 8 weeks after induction of demyelination. Furthermore,
569 unlike mouse lesions (Saraswat et al., 2021b), the transcriptional regulator Prrx1 was specifically
570 upregulated in numerous OPCs at the lesion edge. Prrx1 expression in human OPCs induces a

571 reversible state of quiescence inhibiting proliferation and thereby preventing efficient myelination
572 (Wang et al., 2018). Prrx1 itself is regulated by both interferon-γ and BMP signaling (Wang et al.,
573 2018, Saraswat et al., 2021b) and increased Prrx1 expression in the rabbit suggest that the lesion
574 environment may differ substantially from the mouse brain. Intriguingly, we also observed
575 prominent examples of cells expressing cytoplasmic Olig2 expression in the rabbit lesion that is
576 associated with an astroglial switch in stem/progenitor cells (Setoguchi, 2004) and observed in
577 rare cells in EAE (Cassiani-Ingoni et al., 2006). This is not observed in mouse lysolecithin lesions
578 and further supports species-specific differences in signaling. Lastly, small rabbit lesions of an
579 equivalent volume to mouse, display similar deficits in OPC recruitment. Intriguingly, OPC
580 proliferation is very low in the rabbit small lesion and contrasts with the rapid proliferation that
581 occurs in mouse. OPC autonomous differences between species have been suggested by several
582 other studies. For example, adult mouse OPCs are more than twice as migratory compared to
583 adult human OPCs (Bribian et al., 2020). Following transplantation human OPCs take 8-12 weeks
584 to generate myelin-forming OLs (Sim et al., 2011), while equivalent rodent cells typically complete
585 the process of differentiation in 3-4 weeks (Baron-Van Evercooren and Blakemore, 2004). Lastly,
586 when human OPCs are transplanted into mouse brain, the human cells outcompete their mouse
587 counterparts suggestive of substantial differences in cell biology and signaling between species
588 (Windrem et al., 2014). Together, these results support the hypothesis that species differences
589 are critical determinants of the OPC response to demyelination.

590 Another defining feature of the rabbit model is the capability to induce large volumes of
591 demyelination, approximately 10-fold larger than typical rodent lesions. To specifically examine
592 the role of lesion volume on OPC recruitment and differentiation, we induced both large (4 mm^3)
593 and small (0.4 mm^3) volume lesions in the rabbit brain. As expected, the smaller lesions displayed
594 accelerated regeneration of OLs with time. However, when OPC recruitment was assessed, we
595 noted a dramatic difference in the rate of proliferation in small vs. large lesions. Small lesions
596 exhibited very limited proliferation (<1% Ki67 among Olig2-expressing) whereas OPCs within
597 large lesions were more proliferative (5-15%). It has been estimated that only 1-3 rounds of
598 division are required to restore OPC density in rodent-sized lesions (Foerster et al., 2020). As
599 such, proliferation may not as important in small lesions. Regardless of lesion volume, OPC
600 recruitment never exceeded normal density. However, we did note a volume-dependent
601 difference in the pattern of gliotic response. While astroglial responses were similar between small
602 and large lesions, we observed a notable decrease in microglial reactivity in small lesions.

603 Several recent studies have increasingly highlighted the role that the innate immune
604 response plays in influencing remyelination (Lloyd and Miron, 2019). In this regard, the rabbit

605 microglial response was distinct from the astrocytic response, in that the intensity of staining
606 demonstrated a clear period of activation that waned after the first few weeks. Both microglial and
607 astrocyte activation was sustained in the lesion core for longer periods than the lesion edge and
608 this correlated with the density and activation state of OPCs in these regions. Proliferating
609 $Sox2^{+}Olig2^{+}$ cells were largely found in those regions with enhanced Iba1 and Gfap staining
610 suggestive that the gliotic core was in part driving the sustained OPC proliferation observed in
611 that region. As observed in rat demyelinating lesions and associated with successful
612 remyelination at the lesion rim, the greatest density of mature OL was observed within regions
613 with the least sustained gliotic response. In addition, cytoplasmic Olig2 staining was relatively
614 commonly at the lesion edge, with peak observations at 8 weeks. Interestingly, we observed a
615 corresponding peak in the density of $Sox2^{+}Olig2^{-}$ cells at 8 weeks post lesion induction.
616 The failure of OPC recruitment in the rabbit recapitulates that observed in the majority of
617 MS lesions and thereby provides a suitable test bed for therapeutic approaches to improve the
618 migration and proliferation of OPCs. Indeed, rabbit OPC recruitment resembles that following
619 lysolecithin-induced demyelination of the non-human primate optic nerve, in that densities of OPC
620 and OL do not return to normal white matter levels at 6 months and demyelination is present a 9
621 months (Sarrazin et al., 2022). In contrast to the macaque, the rabbit is substantially more cost-
622 effective and accessible to most neuroscience laboratories. As such, we propose that the
623 simplicity and accessibly of the rabbit model along with the clear differences in lesion environment
624 and patterns of OPC recruitment and differentiation will provide a vital complementary approach
625 for preclinical testing of remyelination therapeutics and aid in the successful development of
626 clinical interventions aimed at promoting myelin regeneration.
627
628 **Conflict of Interest:** The authors declare no competing financial interests.
629 **Author Contributions:**
630 Conception and design of the study: FJS and JJMC. Acquisition and analysis of data: all authors.
631 Drafting the manuscript or figures: FJS and JJMC. Study supervision: FJS.

632 **REFERENCES**

633 ABSINTA, M., MARIC, D., GHARAGOZLOO, M., GARTON, T., SMITH, M. D., JIN, J.,
634 FITZGERALD, K. C., SONG, A., LIU, P., LIN, J. P., WU, T., JOHNSON, K. R.,
635 MCGAVERN, D. B., SCHAFER, D. P., CALABRESI, P. A. & REICH, D. S. 2021. A
636 lymphocyte-microglia-astrocyte axis in chronic active multiple sclerosis. *Nature,* 597**,** 709-
637 714.

638 BARON-VAN EVERCOOREN, A. & BLAKEMORE, W. F. 2004. Remyelination through
639 Engraftment. *In:* LAZZARINI, R. A., GRIFFIN, J. W., LASSMAN, H., NAVE, K.-A., MILLER,
640 R. & TRAPP, B. D. (eds.) *Myelin Biology and Disorders.* San Diego: Academic Press.

641 BLAKEMORE, W. F. 1978. Observations on remyelination in the rabbit spinal cord following
642 demyelination induced by lysolecithin. *Neuropathol Appl Neurobiol,* 4**,** 47-59.

643 BOYD, A., ZHANG, H. & WILLIAMS, A. 2013. Insufficient OPC migration into demyelinated
644 lesions is a cause of poor remyelination in MS and mouse models. *Acta Neuropathol,* 125**,**
645 841-59.

646 BRIBIAN, A., MEDINA-RODRIGUEZ, E. M., JOSA-PRADO, F., GARCIA-ALVAREZ, I., MACHIN-
647 DIAZ, I., ESTEBAN, P. F., MURCIA-BELMONTE, V., VEGA-ZELAYA, L., PASTOR, J.,
648 GARRIDO, L. & DE CASTRO, F. 2020. Functional Heterogeneity of Mouse and Human
649 Brain OPCs: Relevance for Preclinical Studies in Multiple Sclerosis. *J Clin Med,* 9.

650 CADAVID, D., BALCER, L., GALETTA, S., AKTAS, O., ZIEMSSEN, T., VANOPDENBOSCH, L.,
651 FREDERIKSEN, J., SKEEN, M., JAFFE, G. J., BUTZKUEVEN, H., ZIEMSSEN, F.,
652 MASSACESI, L., CHAI, Y., XU, L., FREEMAN, S. & INVESTIGATORS, R. S. 2017. Safety
653 and efficacy of opicinumab in acute optic neuritis (RENEW): a randomised, placebo-
654 controlled, phase 2 trial. *Lancet Neurol,* 16**,** 189-199.

655 CADAVID, D., MELLION, M., HUPPERTS, R., EDWARDS, K. R., CALABRESI, P. A.,
656 DRULOVIĆ, J., GIOVANNONI, G., HARTUNG, H. P., ARNOLD, D. L., FISHER, E.,
657 RUDICK, R., MI, S., CHAI, Y., LI, J., ZHANG, Y., CHENG, W., XU, L., ZHU, B., GREEN,
658 S. M., CHANG, I., DEYKIN, A. & SHEIKH, S. I. 2019. Safety and efficacy of opicinumab
659 in patients with relapsing multiple sclerosis (SYNERGY): a randomised, placebo-
660 controlled, phase 2 trial. *Lancet Neurol,* 18**,** 845-856.

661 CASSIANI-INGONI, R., COKSAYGAN, T., XUE, H., REICHERT-SCRIVNER, S. A., WIENDL, H.,
662 RAO, M. S. & MAGNUS, T. 2006. Cytoplasmic translocation of Olig2 in adult glial
663 progenitors marks the generation of reactive astrocytes following autoimmune
664 inflammation. *Exp Neurol,* 201**,** 349-58.

665 CHARI, D. M. & BLAKEMORE, W. F. 2002. Efficient recolonisation of progenitor-depleted areas
666 of the CNS by adult oligodendrocyte progenitor cells. *Glia,* 37**,** 307-13.
667 CONFAVREUX, C., VUKUSIC, S., MOREAU, T. & ADELEINE, P. 2000. Relapses and
668 progression of disability in multiple sclerosis. *N Engl J Med,* 343**,** 1430-8.
669 DIETZ, K. C., POLANCO, J. J., POL, S. U. & SIM, F. J. 2016. Targeting human oligodendrocyte
670 progenitors for myelin repair. *Exp Neurol,* 283**,** 489-500.
671 DORRIER, C. E., ARAN, D., HAENELT, E. A., SHEEHY, R. N., HOI, K. K., PINTARIC, L., CHEN,
672 Y., LIZAMA, C. O., CAUTIVO, K. M., WEINER, G. A., POPKO, B., FANCY, S. P. J.,
673 ARNOLD, T. D. & DANEMAN, R. 2021. CNS fibroblasts form a fibrotic scar in response
674 to immune cell infiltration. *Nat Neurosci,* 24**,** 234-244.
675 FANCY, S. P., BARANZINI, S. E., ZHAO, C., YUK, D. I., IRVINE, K. A., KAING, S., SANAI, N.,
676 FRANKLIN, R. J. & ROWITCH, D. H. 2009. Dysregulation of the Wnt pathway inhibits
677 timely myelination and remyelination in the mammalian CNS. *Genes Dev,* 23**,** 1571-85.
678 FANCY, S. P., CHAN, J. R., BARANZINI, S. E., FRANKLIN, R. J. & ROWITCH, D. H. 2011. Myelin
679 regeneration: a recapitulation of development? *Annu Rev Neurosci,* 34**,** 21-43.
680 FANCY, S. P., ZHAO, C. & FRANKLIN, R. J. 2004. Increased expression of Nkx2.2 and Olig2
681 identifies reactive oligodendrocyte progenitor cells responding to demyelination in the
682 adult CNS. *Mol Cell Neurosci,* 27**,** 247-54.
683 FOERSTER, S., NEUMANN, B., MCCLAIN, C., DI CANIO, L., CHEN, C. Z., REICH, D. S.,
684 SIMONS, B. D. & FRANKLIN, R. J. 2020. Proliferation is a requirement for differentiation
685 of oligodendrocyte progenitor cells during CNS remyelination. *bioRxiv***,**
686 2020.05.21.108373.
687 FOSTER, R. E., KOCSIS, J. D., MALENKA, R. C. & WAXMAN, S. G. 1980. Lysophosphatidyl
688 choline-induced focal demyelination in the rabbit corpus callosum. Electron-microscopic
689 observations. *J Neurol Sci,* 48**,** 221-31.
690 FRANKLIN, R. J. & GOLDMAN, S. A. 2015. Glia Disease and Repair-Remyelination. *Cold Spring*
691 *Harb Perspect Biol,* 7**,** a020594.
692 FRANKLIN, R. J. M. & FFRENCH-CONSTANT, C. 2017. Regenerating CNS myelin - from
693 mechanisms to experimental medicines. *Nat Rev Neurosci,* 18**,** 753-769.
694 FRANKLIN, R. J. M., FRISÉN, J. & LYONS, D. A. 2021. Revisiting remyelination: Towards a
695 consensus on the regeneration of CNS myelin. *Semin Cell Dev Biol,* 116**,** 3-9.
696 GREEN, A. J., GELFAND, J. M., CREE, B. A., BEVAN, C., BOSCARDIN, W. J., MEI, F., INMAN,
697 J., ARNOW, S., DEVEREUX, M., ABOUNASR, A., NOBUTA, H., ZHU, A., FRIESSEN,
698 M., GERONA, R., VON BUDINGEN, H. C., HENRY, R. G., HAUSER, S. L. & CHAN, J. R.

2017. Clemastine fumarate as a remyelinating therapy for multiple sclerosis (ReBUILD): a randomised, controlled, double-blind, crossover trial. *Lancet,* 390**,** 2481-2489.

HES, K., STAROST, L., KIERAN, N. W., THOMAS, C., VINCENTEN, M. C. J., ANTEL, J., MARTINO, G., HUITINGA, I., HEALY, L. & KUHLMANN, T. 2020. Lesion stage-dependent causes for impaired remyelination in MS. *Acta Neuropathologica,* 140**,** 359-375.

HUGHES, E. G., KANG, S. H., FUKAYA, M. & BERGLES, D. E. 2013. Oligodendrocyte progenitors balance growth with self-repulsion to achieve homeostasis in the adult brain. *Nat Neurosci,* 16**,** 668-76.

KERSTETTER, A. E., PADOVANI-CLAUDIO, D. A., BAI, L. & MILLER, R. H. 2009. Inhibition of CXCR2 signaling promotes recovery in models of multiple sclerosis. *Exp Neurol,* 220**,** 44-56.

KUCHAROVA, K., CHANG, Y., BOOR, A., YONG, V. W. & STALLCUP, W. B. 2011. Reduced inflammation accompanies diminished myelin damage and repair in the NG2 null mouse spinal cord. *J Neuroinflammation,* 8**,** 158.

KUCHAROVA, K. & STALLCUP, W. B. 2015. NG2-proteoglycan-dependent contributions of oligodendrocyte progenitors and myeloid cells to myelin damage and repair. *J Neuroinflammation,* 12**,** 161.

KUHLMANN, T., MIRON, V., CUI, Q., WEGNER, C., ANTEL, J. & BRUCK, W. 2008. Differentiation block of oligodendroglial progenitor cells as a cause for remyelination failure in chronic multiple sclerosis. *Brain,* 131**,** 1749-58.

LIN, W., KEMPER, A., DUPREE, J. L., HARDING, H. P., RON, D. & POPKO, B. 2006. Interferon-gamma inhibits central nervous system remyelination through a process modulated by endoplasmic reticulum stress. *Brain,* 129**,** 1306-18.

LLOYD, A. F. & MIRON, V. E. 2019. The pro-remyelination properties of microglia in the central nervous system. *Nature Reviews Neurology,* 15**,** 447-458.

LUBETZKI, C., SOL-FOULON, N. & DESMAZIERES, A. 2020. Nodes of Ranvier during development and repair in the CNS. *Nat Rev Neurol,* 16**,** 426-439.

LUCCHINETTI, C., BRUCK, W., PARISI, J., SCHEITHAUER, B., RODRIGUEZ, M. & LASSMANN, H. 1999. A quantitative analysis of oligodendrocytes in multiple sclerosis lesions. A study of 113 cases. *Brain,* 122 (Pt 12)**,** 2279-95.

MASON, J. L., TOEWS, A., HOSTETTLER, J. D., MORELL, P., SUZUKI, K., GOLDMAN, J. E. & MATSUSHIMA, G. K. 2004. Oligodendrocytes and progenitors become progressively depleted within chronically demyelinated lesions. *Am J Pathol,* 164**,** 1673-82.

732 MEI, F., FANCY, S. P. J., SHEN, Y. A., NIU, J., ZHAO, C., PRESLEY, B., MIAO, E., LEE, S.,
733 MAYORAL, S. R., REDMOND, S. A., ETXEBERRIA, A., XIAO, L., FRANKLIN, R. J. M.,
734 GREEN, A., HAUSER, S. L. & CHAN, J. R. 2014. Micropillar arrays as a high-throughput
735 screening platform for therapeutics in multiple sclerosis. *Nat Med,* 20**,** 954-960.
736 MELLION, M., EDWARDS, K. R., HUPPERTS, R., DRULOVIC, J., MONTALBAN, X., HARTUNG,
737 H. P., BROCHET, B., CALABRESI, P. A., RUDICK, R., IBRAHIM, A., ZHANG, Y. W., XU,
738 L. & CADAVID, D. 2017. Efficacy Results from the Phase 2b SYNERGY Study: Treatment
739 of Disabling Multiple Sclerosis with the Anti-LINGO-1 Monoclonal Antibody Opicinumab.
740 *Neurology,* 88.
741 MI, S., MILLER, R. H., LEE, X., SCOTT, M. L., SHULAG-MORSKAYA, S., SHAO, Z., CHANG,
742 J., THILL, G., LEVESQUE, M., ZHANG, M., HESSION, C., SAH, D., TRAPP, B., HE, Z.,
743 JUNG, V., MCCOY, J. M. & PEPINSKY, R. B. 2005. LINGO-1 negatively regulates
744 myelination by oligodendrocytes. *Nat Neurosci,* 8**,** 745-51.
745 MOLL, N. M., HONG, E., FAUVEAU, M., NARUSE, M., KERNINON, C., TEPAVCEVIC, V.,
746 KLOPSTEIN, A., SEILHEAN, D., CHEW, L. J., GALLO, V. & NAIT OUMESMAR, B. 2013.
747 SOX17 is expressed in regenerating oligodendrocytes in experimental models of
748 demyelination and in multiple sclerosis. *Glia,* 61**,** 1659-72.
749 PENDERIS, J., SHIELDS, S. A. & FRANKLIN, R. J. 2003. Impaired remyelination and depletion
750 of oligodendrocyte progenitors does not occur following repeated episodes of focal
751 demyelination in the rat central nervous system. *Brain,* 126**,** 1382-91.
752 PIATON, G., AIGROT, M. S., WILLIAMS, A., MOYON, S., TEPAVCEVIC, V., MOUTKINE, I.,
753 GRAS, J., MATHO, K. S., SCHMITT, A., SOELLNER, H., HUBER, A. B., RAVASSARD,
754 P. & LUBETZKI, C. 2011. Class 3 semaphorins influence oligodendrocyte precursor
755 recruitment and remyelination in adult central nervous system. *Brain,* 134**,** 1156-67.
756 PRINEAS, J., RAINE, C. S. & WÍSNIEWSKI, H. 1969. An ultrastructural study of experimental
757 demyelination and remyelination. 3. Chronic experimental allergic encephalomyelitis in the
758 central nervous system. *Lab Invest,* 21**,** 472-83.
759 ROSEN, G. D. & HARRY, J. D. 1990. Brain volume estimation from serial section measurements:
760 a comparison of methodologies. *J Neurosci Methods,* 35**,** 115-24.
761 ROSENBERG, S. S., KELLAND, E. E., TOKAR, E., DE LA TORRE, A. R. & CHAN, J. R. 2008.
762 The geometric and spatial constraints of the microenvironment induce oligodendrocyte
763 differentiation. *Proc Natl Acad Sci U S A,* 105**,** 14662-7.
764 SARASWAT, D., SHAYYA, H. J., POLANCO, J. J., TRIPATHI, A., WELLIVER, R. R., POL, S. U.,
765 SEIDMAN, R. A., BROOME, J. E., O'BARA, M. A., VAN KUPPERVELT, T. H., PHILLIPS,

766 J. J., DUTTA, R. & SIM, F. J. 2021a. Overcoming the inhibitory microenvironment
767 surrounding oligodendrocyte progenitor cells following experimental demyelination. *Nat*
768 *Commun,* 12**,** 1923.
769 SARASWAT, D., WELLIVER, R. R., RAVICHANDAR, R., TRIPATHI, A., POLANCO, J. J.,
770 BROOME, J., HURLEY, E., DUTTA, R., FELTRI, M. L. & SIM, F. J. 2021b. Heparanome-
771 Mediated Rescue of Oligodendrocyte Progenitor Quiescence following Inflammatory
772 Demyelination. *J Neurosci,* 41**,** 2245-2263.
773 SARRAZIN, N., CHAVRET-RECULON, E., BACHELIN, C., FELFLI, M., ARAB, R., GILARDEAU,
774 S., BRAZHNIKOVA, E., DUBUS, E., YAHA-CHERIF, L., LORENCEAU, J., PICAUD, S.,
775 ROSOLEN, S., MOISSONNIER, P., POUGET, P. & BARON-VAN EVERCOOREN, A.
776 2022. Failed remyelination of the nonhuman primate optic nerve leads to axon
777 degeneration, retinal damages, and visual dysfunction. *Proc Natl Acad Sci U S A,* 119**,**
778 e2115973119.
779 SERWANSKI, D. R., RASMUSSEN, A. L., BRUNQUELL, C. B., PERKINS, S. S. & NISHIYAMA,
780 A. 2018. Sequential Contribution of Parenchymal and Neural Stem Cell-Derived
781 Oligodendrocyte Precursor Cells toward Remyelination. *Neuroglia,* 1**,** 91-105.
782 SETOGUCHI, T. 2004. Nuclear export of OLIG2 in neural stem cells is essential for ciliary
783 neurotrophic factor-induced astrocyte differentiation. *The Journal of Cell Biology,* 166**,**
784 963-968.
785 SIM, F. J., MCCLAIN, C. R., SCHANZ, S. J., PROTACK, T. L., WINDREM, M. S. & GOLDMAN,
786 S. A. 2011. CD140a identifies a population of highly myelinogenic, migration-competent
787 and efficiently engrafting human oligodendrocyte progenitor cells. *Nat Biotechnol,* 29**,** 934-
788 41.
789 SIM, F. J., ZHAO, C., PENDERIS, J. & FRANKLIN, R. J. 2002. The age-related decrease in CNS
790 remyelination efficiency is attributable to an impairment of both oligodendrocyte progenitor
791 recruitment and differentiation. *J Neurosci,* 22**,** 2451-9.
792 TEPAVCEVIC, V., KERNINON, C., AIGROT, M. S., MEPPIEL, E., MOZAFARI, S., ARNOULD-
793 LAURENT, R., RAVASSARD, P., KENNEDY, T. E., NAIT-OUMESMAR, B. & LUBETZKI,
794 C. 2014. Early netrin-1 expression impairs central nervous system remyelination. *Ann*
795 *Neurol,* 76**,** 252-68.
796 ULRICH, R., SEELIGER, F., KREUTZER, M., GERMANN, P. G. & BAUMGARTNER, W. 2008.
797 Limited remyelination in Theiler's murine encephalomyelitis due to insufficient
798 oligodendroglial differentiation of nerve/glial antigen 2 (NG2)-positive putative
799 oligodendroglial progenitor cells. *Neuropathol Appl Neurobiol,* 34**,** 603-20.

800 WANG, J., SARASWAT, D., SINHA, A. K., POLANCO, J., DIETZ, K., O'BARA, M. A., POL, S. U.,
801 SHAYYA, H. J. & SIM, F. J. 2018. Paired Related Homeobox Protein 1 Regulates
802 Quiescence in Human Oligodendrocyte Progenitors. *Cell Rep,* 25**,** 3435-3450 e6.
803 WAXMAN, S. G., KOCSIS, J. D. & NITTA, K. C. 1979. Lysophosphatidyl choline-induced focal
804 demyelination in the rabbit corpus callosum. Light-microscopic observations. *J Neurol Sci,*
805 44**,** 45-53.
806 WILLIAMS, R. M., LEES, M. B., CAMBI, F. & MACKLIN, W. B. 1982. Chronic Experimental
807 Allergic Encephalomyelitis Induced in Rabbits with Bovine White Matter Proteolipid
808 Apoprotein. *Journal of Neuropathology & Experimental Neurology,* 41**,** 508-521.
809 WINDREM, M. S., SCHANZ, S. J., MORROW, C., MUNIR, J., CHANDLER-MILITELLO, D.,
810 WANG, S. & GOLDMAN, S. A. 2014. A competitive advantage by neonatally engrafted
811 human glial progenitors yields mice whose brains are chimeric for human glia. *J Neurosci,*
812 34**,** 16153-61.
813 WOLSWIJK, G. 1998. Chronic stage multiple sclerosis lesions contain a relatively quiescent
814 population of oligodendrocyte precursor cells. *J Neurosci,* 18**,** 601-9.
815 WOODRUFF, R. H., FRUTTIGER, M., RICHARDSON, W. D. & FRANKLIN, R. J. 2004. Platelet-
816 derived growth factor regulates oligodendrocyte progenitor numbers in adult CNS and
817 their response following CNS demyelination. *Mol Cell Neurosci,* 25**,** 252-62.
818 XING, Y. L., CHUANG, B. H. A., POH, J., MORADI, K., MITEW, S., KILPATRICK, T. J., OSANAI,
819 Y. & MERSON, T. D. 2021. A Novel Pharmacogenetic Model for Highly Efficient Ablation
820 of Oligodendrocyte Progenitor Cells in the Adult Mouse CNS. *bioRxiv***,**
821 2021.05.13.443012.
822 ZAWADZKA, M., RIVERS, L. E., FANCY, S. P., ZHAO, C., TRIPATHI, R., JAMEN, F., YOUNG,
823 K., GONCHAREVICH, A., POHL, H., RIZZI, M., ROWITCH, D. H., KESSARIS, N.,
824 SUTER, U., RICHARDSON, W. D. & FRANKLIN, R. J. 2010. CNS-resident glial
825 progenitor/stem cells produce Schwann cells as well as oligodendrocytes during repair of
826 CNS demyelination. *Cell Stem Cell,* 6**,** 578-90.
827 ZHAO, C., MA, D., ZAWADZKA, M., FANCY, S. P., ELIS-WILLIAMS, L., BOUVIER, G.,
828 STOCKLEY, J. H., DE CASTRO, G. M., WANG, B., JACOBS, S., CASACCIA, P. &
829 FRANKLIN, R. J. 2015. Sox2 Sustains Recruitment of Oligodendrocyte Progenitor Cells
830 following CNS Demyelination and Primes Them for Differentiation during Remyelination.
831 *J Neurosci,* 35**,** 11482-99.

832

833 **FIGURE LEGENDS**

834 **Figure 1. Large regions of demyelination following injection of lysolecithin into rabbit**
835 **subcortical white matter persisted for at least 6 months. A**, Scale diagram representing
836 injection sites and white matter tract size (mouse included for reference). **B**, Lysolecithin-induced
837 lesion at 14 days post-lesion (dpl) in the rabbit stained for FloroMyelin (FM, red) and 4',6'-
838 diamidino-2-phenylindole (DAPI, blue). White dotted line indicates lesion border. **C-D**, Lesion
839 volume (**C**) and maximal cross-sectional area (**D**) of lesions overtime. Mean ± SEM shown. Scale:
840 5 mm (**A**), 500 µm (**D**).

841

842 **Figure 2. Insufficient oligodendrocyte progenitor cell recruitment and mature**
843 **oligodendrocyte generation following demyelination in rabbit white matter. A**,
844 Oligodendrocyte progenitor cells (OPCs), and mature oligodendrocytes (OL) were identified as
845 $Olig2^{+}CC1^{-}$ and $Olig2^{+}CC1^{+}$, respectively. Insert shows a high magnification image of a $CC1^{+}$
846 (green) mature OL. **B**, Olig2 (red) was used to identify total oligodendrocyte lineage cell density
847 which was significantly depressed at 7 and 21 days post-lesion (dpl), but recovered by 56 dpl (n
848 = 3-6, One-way ANOVA, F (5, 23) = 0.44, $p < 0.0001$). **C**, Interestingly, OPC ($Olig2^{+}CC1^{-}$) density
849 did not significantly increase above that of normal white matter (NWM) at any timepoint (n = 3-6,
850 One-way ANOVA, F (5, 22) = 0.83, $p = 0.008$). **D**, Additionally, $CC1^{+}$ mature OL densities failed
851 to recover, remaining significantly below that of NWM even at 180 dpl (n = 3-6, One-way ANOVA,
852 F (5, 22) = 0.57, $p < 0.0001$). **E**, The percentage of $Olig2^{+}$ cells that were differentiated was also
853 depressed (n= 3-6, One-way ANOVA, F (5, 22) = 0.87, $p < 0.0001$). Tukey's multiple comparisons
854 post-test. *, **, ***, and **** indicate $p \leq 0.05, 0.01, 0.001$, and 0.0001, respectively. Pairwise
855 significance shown between NWM and each respective timepoint. Dashed lines on graph
856 represent mean of NWM. Mean ± SEM shown. Scale: 50 µm (**A**), 10 µm (**A**, insert).

857

858 **Figure 3. Abundant oligodendrocyte progenitor cell activation but disproportionately low**
859 **proliferation following injury. A-D**, Representative images of normal white matter (**A**), or lesion
860 at 14 days post-lesion (dpl) (**B**), 56 dpl (**C**), 180 dpl (**D**). Activated $Sox2^{+}$ OPCs (cyan), proliferative
861 $Ki67^{+}$ OPCs (green) were identified by colocalization with Olig2 (red). Additionally, Sox2 has been
862 noted to be expressed by a subpopulation of astrocytes (Zhao et al., 2015) which are identified
863 as $Sox2^{+}Olig2^{-}$ cells. Insert shows high magnification of labelled cells. **E**, The density of activated
864 $Sox2^{+}$ OPCs increased following demyelination, which peaked at 14 dpl (One-way ANOVA, F (5,
865 21) = 0.86, $p < 0.0001$). **F**, Correspondingly, the proportion of $Ki67^{+}$ proliferating OPCs also
866 peaked at 14 dpl. Densities of both active and proliferative OPCs gradually decreased to normal

867 levels by 180 dpl (n= 3-6, One-way ANOVA, F (5, 21) = 2.05, p = 0.005). **G**, At 7dpl, the proportion
868 of $Sox2^+$ activated OPCs that are proliferating is not significantly increased relative to normal white
869 matter, and did not peak until 56 dpl (n= 3-6, One-way ANOVA, F (5, 21) = 1.02, p = 0.01). **H-I**,
870 Additionally, there was an accumulation of $Sox2^+Olig2^-$ astrocytes, confirmed with Gfap (**H**),
871 where densities peaked at 56 dpl (One-way ANOVA, F (5, 22) = 1.92, p = 0.0003) (**I**). Tukey's
872 multiple comparisons post-test. *, **, ***, and **** indicate p ≤ 0.05, 0.01, 0.001, and 0.0001,
873 respectively. Dashed lines on graph represent mean of normal white matter. Mean ± SEM shown.
874 Scale: 200 µm (**A**), 10 µm (**A**, inserts), 5 µm (**H**).
875
876 **Figure 4. Large lesions displayed abundant gliosis, with the microglia/macrophage**
877 **response greatest at early timepoints. A-D**, Iba1 (red), and Gfap (green) were used as markers
878 of microglia/macrophages and astrocytes, respectively, with nuclei labeled with DAPI (blue).
879 Lesion borders (white dashed line) and perilesion white matter (PLWM) outlines are shown (blue
880 dashed line). Inserts show higher power confocal images of areas outlined with white box. **E**, Iba1
881 mean fluorescent intensity (MFI) peaked at 7 dpl, and gradually decreased towards 180 days
882 post-lesion (dpl) (n = 4-29, One-way ANOVA, F (5, 57) = 3.13, p = 0.015). The corpus callosum
883 was considered normal appearing white matter (NAWM) for quantitative comparisons and to
884 control for batch and animal staining variability. **F**, Total $Gfap^+$ area was quantified and shown as
885 a proportion of total lesion area, and was elevated above NAWM at all timepoints (n = 4-29, One-
886 way ANOVA, F (5, 50) = 2.92, p < 0.0001). **G-H**, Both Iba1 MFI and Gfap % area was also
887 increased in the PLWM at 21 dpl, and decreased at later timepoints (n = 4-29, one-way ANOVA).
888 Tukey's multiple comparisons post-test. *, **, ***, and **** indicate p ≤ 0.05, 0.01, 0.001, and
889 0.0001, respectively. Pairwise significance shown between normal white matter (NWM) and
890 respective timepoint. Dashed lines on graph represent mean of NWM (n = 3). Mean ± SEM shown.
891 Scale: 500 µm (**A-D**), 25 µm (**A**, inserts, **I-K**).
892
893 **Figure 5. The perilesion white matter displayed hypercellularity and disturbed myelin**
894 **structure. A**, Evolution of lysolecithin-induced lesions in the rabbit over time stained for
895 FloroMyelin (FM, red) and DAPI (blue). White dashed line indicates lesion bounds. An area of
896 hypercellularity extending past the lesion boundary was noted (blue dashed line). **B-C**,
897 Comparison of normal (**B**) and lesion nuclei density at 56 dpl (**D**) (DAPI, cyan). The density of
898 nuclei following lesion induction is clearly increased relative to matched normal white matter and
899 can be further subdivided at the FM-defined border corresponding with an additional increase in
900 cell density (**C**, white dashed line). **D**, Comparison of mean maximal cross-sectional area of lesion

901 (FM-defined border) and perilesion white matter (PLWM) areas (DAPI hypercellularity-defined
902 border). **E-F**, Representative confocal images of normal white matter stained for myelin, and
903 axonal markers. **G-H**, Following demyelination at 7 to 56 dpl, lesions were imaged by widefield
904 epifluorescence shown in the left panel. **G'-H'**, Higher power confocal images of the area outlined
905 with the white box are shown in the right panel. At 7 dpl, myelin basic protein (Mbp, gray) staining
906 demonstrated myelin loss and degeneration within the lesion, and Mbp levels remain depressed
907 over time (**G**). Axons, stained with neurofilament (NF, green), persist within the lesion bounds
908 even at 56 dpl. Axonal injury (App, red) is evident at 7dpl but is reduced thereafter following
909 demyelination (**H**). Dashed lines on graph represent mean of normal white matter. Mean ± SEM
910 shown. dpl, days post lesion. Scale: 500 μm (**A, G-H**), 200 μm (**C**), 25 μm (**E, G'-H'**).
911
912 **Figure 6. Mature oligodendrocyte density was reduced in the perilesion white matter, with**
913 **increased expression of Prrx1 among OPCs at the lesion edge. A-E**, Three regions were
914 defined for regional analysis: perilesion white matter (PLWM) (light green dashed line), lesion
915 edge (green dashed line), and lesion core (dark green dashed line). PLWM was defined as an
916 area of mild hypercellularity (defined using DAPI) extending past the lesion border. The lesion
917 proper was divided into the edge and core regions, with the edge defined as the outermost 75μm
918 rim. Cross-sectional columns of a 56 dpl lesion covering the various regions stained for
919 solochrome cyanine (**A**), mature oligodendrocytes ($Olig2^+CC1^+$) (**B**), active oligodendrocyte
920 progenitor cell ($Olig2^+Ki67^+$) (**C**), proliferative OPCs ($Olig2^+Ki67^+$) (**D**), and $Gfap^+$ astrocytes (**E**).
921 **F-H**, Quantification of cell density and/or proportion of total oligodendrocyte linage cells between
922 regions for mature OLs ($Olig2^+CC1^{+,}$ **F**), OPCs ($Olig2^+CC1^-$, **G**), and activated OPCs ($Olig2^+Sox2^+$,
923 **H**). Horizontal dotted lines represent mean ± SEM of the corresponding cellular density of normal
924 white matter (n = 3 rabbits). Two-way ANOVA was performed across all time points (TME: time
925 main effect) and comparing regions (RME: regional main effect). **I-K**, a combination of *in situ*
926 hybridization and immunohistochemistry was used to label Prrx1 mRNA (gray) and Olig2 protein
927 (red). Prrx1 expression was increased among the increased density of $Olig2^+$ cells found at the
928 lesion edge at 14 dpl. By 56 dpl, the expression of Prrx1 had decreased among $Olig2^+$ cells.
929 Arrowheads indicate coexpressing of Olig2 and Prrx1.**L**, an example of a cytoplasmic Olig2
930 immunoreactive cell at 56 dpl. These cells were relatively common observation following
931 demyelination (~1-2 cells per section, most commonly observed at 56 dpl). dpl, days post-lesion.
932 Mean ± SEM shown. Scale: 200 μm (**E, N-O**), 10 μm (**M**).
933

934 **Figure 7. Small, murine sized, lesions produced in the rabbit displayed a lesser**
935 **microglia/macrophage response.** Small (0.35 µL) (**A-C**) and large (5 µL) (**D-F**) volume lesions
936 were created via stereotaxic injection lysolecithin, and stained for Gfap (green), Iba1(red) and
937 DAPI (blue). White dashed lines indicate lesion border. **G**, As expected, 0.35 µL injections of
938 lysolecithin produced lesions with significantly smaller volumes as compared to 5 µL at every time
939 point (n= 4-9, two-way ANOVA, volume factor $F(1,33) = 72.5$, $p < 0.0001$). **H**, Small and large
940 volume lesions displayed similar levels of hypercellularity ($DAPI^+/mm^2$). **I**, Small and large lesions
941 also displayed a similar astrocyte response ($Gfap^+$ area/total lesion area) (n= 4-9, two-way
942 ANOVA, volume factor $F(1,32) = 0.05$, $p > 0.05$). **J**, However, Iba1 MFI was significantly greater
943 in large volume lesions compared to small lesions (n= 4-9, two-way ANOVA, volume factor
944 $F(1,28) = 17.39$, $p = 0.0003$). Šídák's multiple comparisons post-test. *, **, ***, and **** indicate p
945 ≤ 0.05, 0.01, 0.001, and 0.0001, respectively. Dashed lines on graph represent mean of normal
946 white matter (n = 3 rabbits). dpl, days post-lesion. Mean ± SEM shown. Scale: 200 µm.
947
948 **Figure 8. Small volume lesions displayed less oligodendrocyte progenitor cell activation**
949 **and improved oligodendrogenesis. A-C**, Activated $Sox2^+$ oligodendrocyte progenitor cells
950 (OPCs) (**B**, cyan), and proliferative $Ki67^+$ OPCs (**C**, green) were identified by colocalization with
951 Olig2 at 14 dpl in small and large volume lesions. Insert shows high magnification of labelled cells.
952 **D**, oligodendrocyte differentiation was assessed by CC1 (green) and Olig2 (red)
953 immunofluorescence. A representative $CC1^+Olig2^+$ cell is shown (**D**, inset). **E**, Small volume
954 lesions had a significantly greater $Olig2^+$ cell density compared to large volume lesions (n = 4-5,
955 two-way ANOVA, volume factor $F(1,22) = 7.3$, $p = 0.013$), however there was no significant
956 difference at any timepoint. **F**, The density of $Sox2^+$ activated OPCs ($Sox2^+Olig2^+$) was
957 significantly greater in large lesions, peaking at 14 dpl in large volume lesions (n = 4-5, two-way
958 ANOVA, volume factor $F(1,21) = 31.3$, $p < 0.0001$). **G**, The proportion of proliferative OPCs
959 ($Ki67^+Olig2^+$) was also significantly increased in large lesions, again peaking at 14 dpl (n = 4-5,
960 two-way ANOVA). **H**, Roughly 20% of activated OPCs in large volume lesions are also
961 proliferating ($Ki67^+Sox2^+Olig2^+$) at 14 dpl, which is significantly increased relative to small lesions
962 where only about 2% of activated OPCs are also proliferating (n = 4-5, two-way ANOVA, volume
963 factor $F(1,21) = 28.4$, $p < 0.0001$). **I**, There were no significant differences between small and
964 large lesions in terms of OPC density ($CC1^-Olig2^+$) (n = 4-5, two-way ANOVA, volume factor
965 $F(1,22) = 0.67$, $p < 0.5$). **J**, Small lesions showed significantly greater densities of mature
966 oligodendrocytes (OL) (volume main effect), gradually increasing towards later timepoints (n = 4-
967 5, two-way ANOVA, volume factor $F(1,22) = 10.7$, $p = 0.004$). **K**, Additionally, a greater proportion

968 of Olig2^{+} cells were differentiated in small lesions vs large lesions (n = 4-5, two-way ANOVA,
969 volume factor F(1,22) = 15.7, p = 0.0007). Šídák's multiple comparisons post-test. *, **, ***, and
970 **** indicate p > 0.05, p ≤ 0.05, 0.01, 0.001, and 0.0001, respectively. Dashed lines on graph
971 represent mean of normal white matter. dpl, days post-lesion. Mean ± SEM shown. Scale: 50 μm
972 (**A-D**), 10 μm (**A-D**, insets).

Figure 1

Scale Bar Fig1A: 500 µm
Scale Bar Fig1B: 5 mm

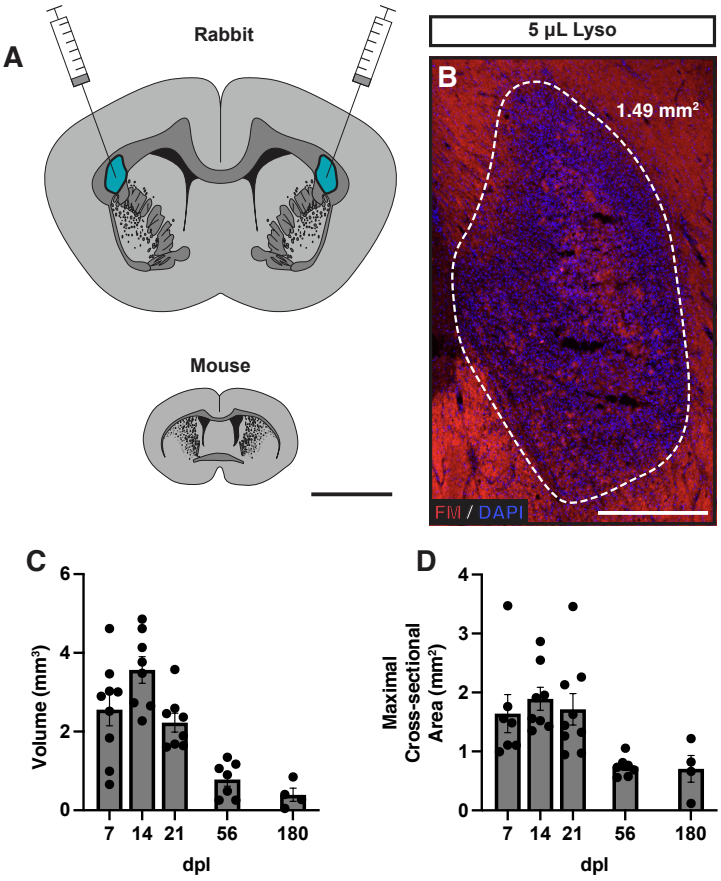

Figure 2

Scale Bar Fig2A inset: 10 µm
Scale Bar Fig2A Whole: 50 µm

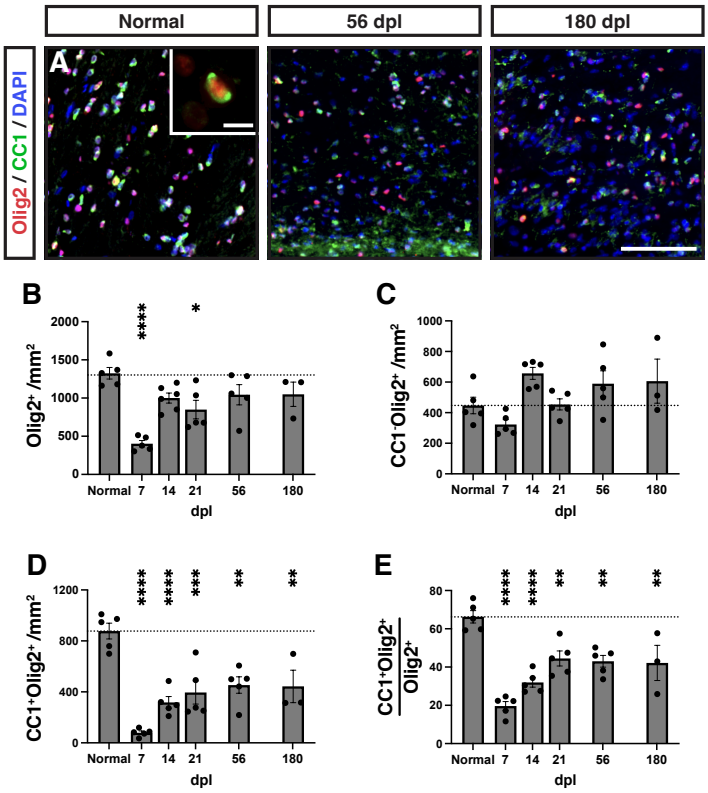

Figure 3

Scale Bar Fig3A inset: 10 µm
Scale Bar Fig3A Whole: 200 µm
Scale Bar Fig3H Whole: 5 µm

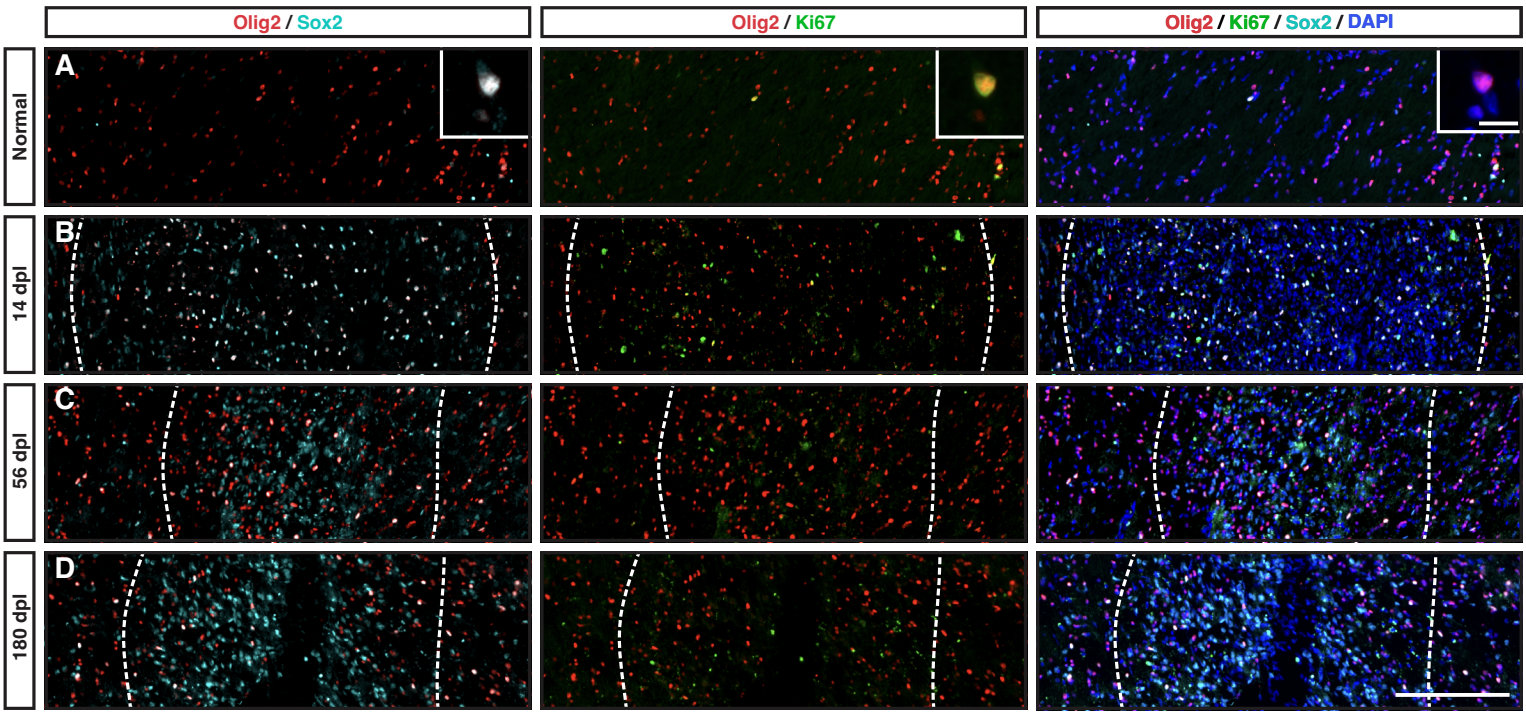

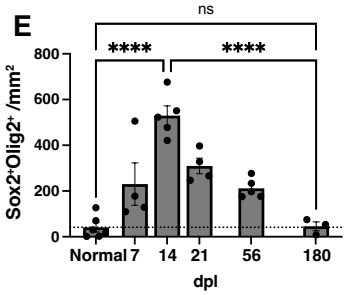

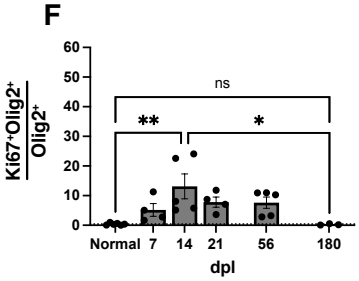

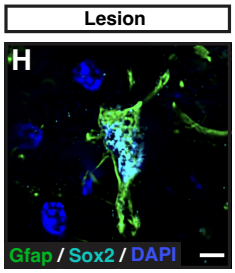

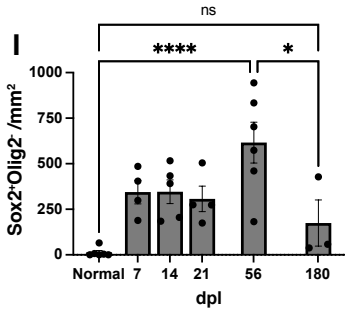

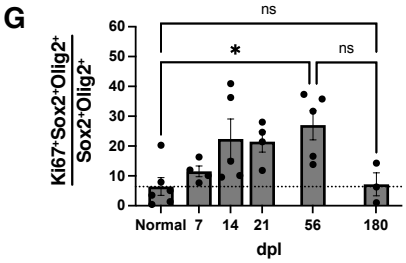

Figure 4

Scale Bar Fig4A inset: 25 µm
Scale Bar Fig4A-D Whole: 500 µm
Scale Bar Fig4I-J : 25 µm
Scale Bar Fig4 : 25 µm

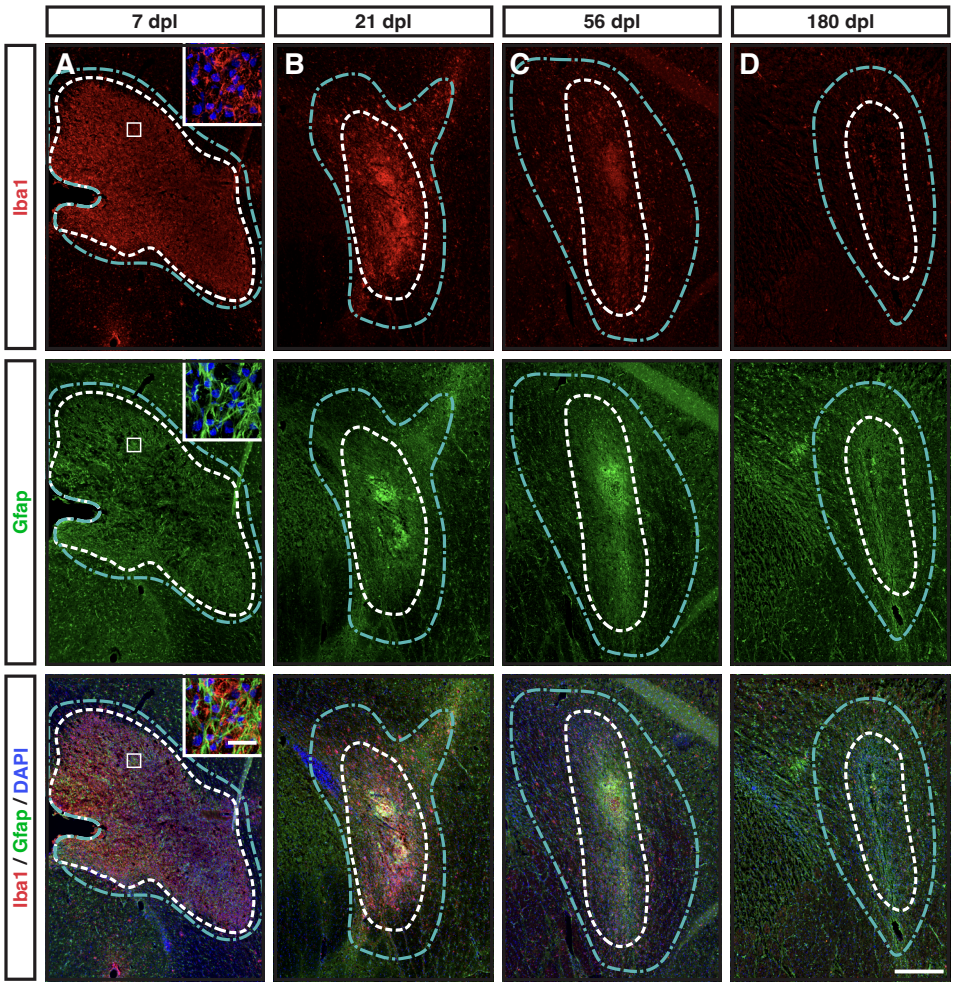

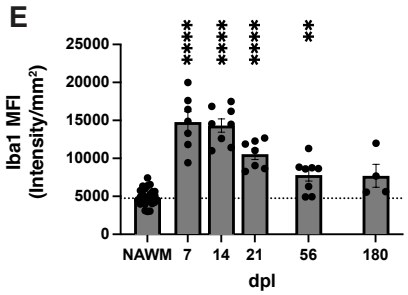

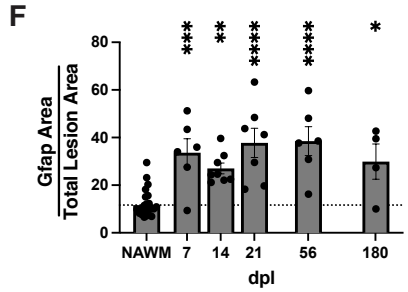

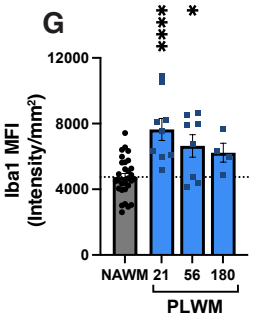

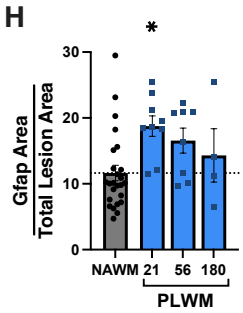

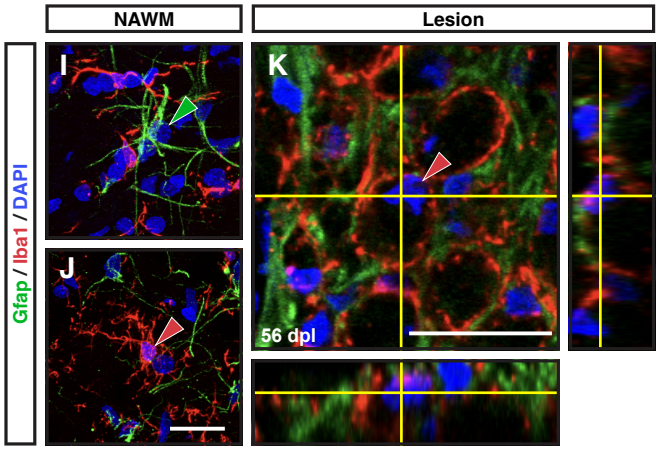

Figure 5

Scale Bar Fig5A: 500 µm
Scale Bar Fig5C: 200 µm
Scale Bar Fig5E-H: Whoel Lesion: 500 µm
Confocal: 25 µm

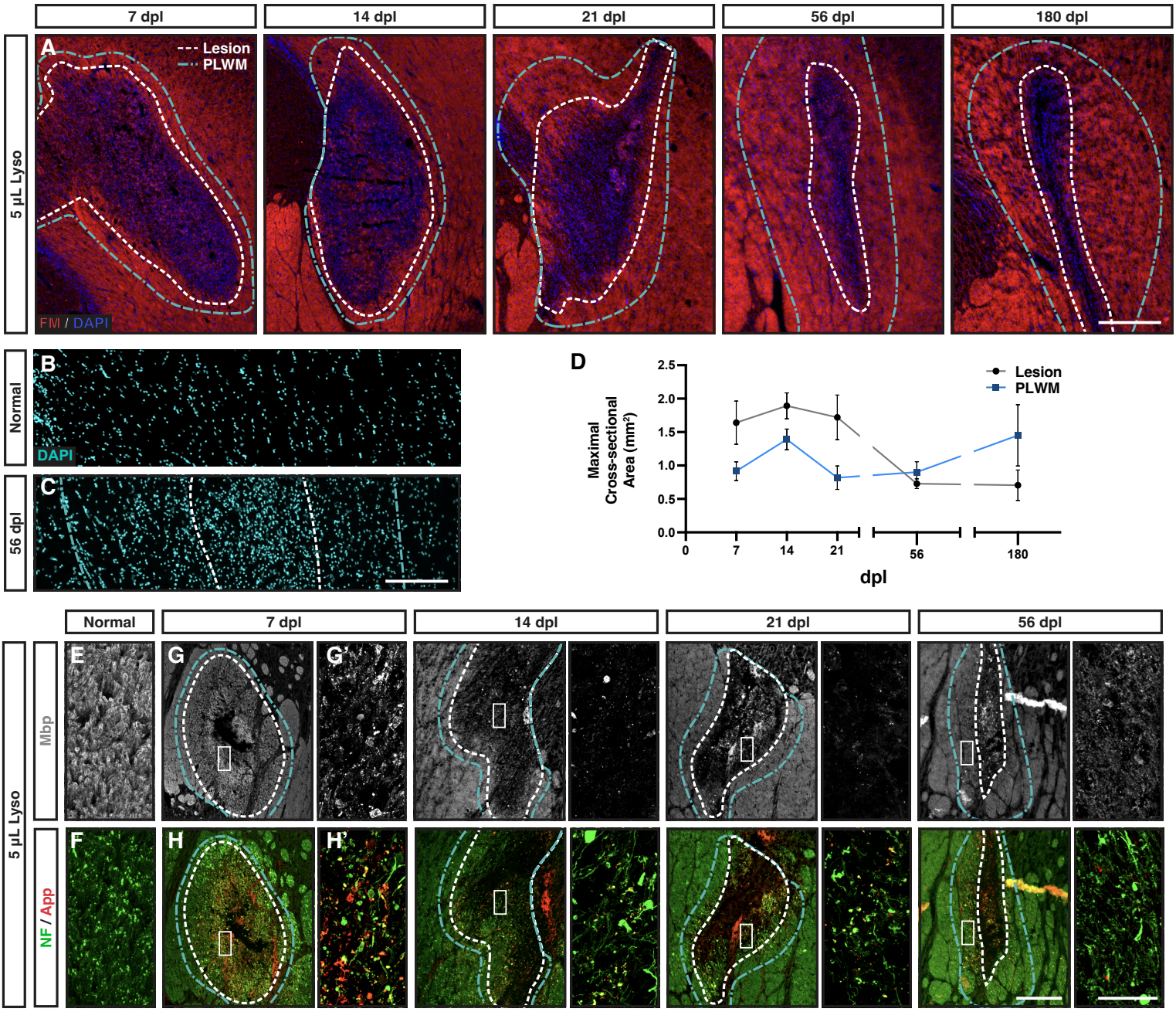

Figure 6

Scale Bar Fig6A-C: 200 µm
Scale Bar Fig6 I: 25 µm
Scale Bar Fig6 J-K: 100 µm
Scale Bar Fig6 L: 15 µm

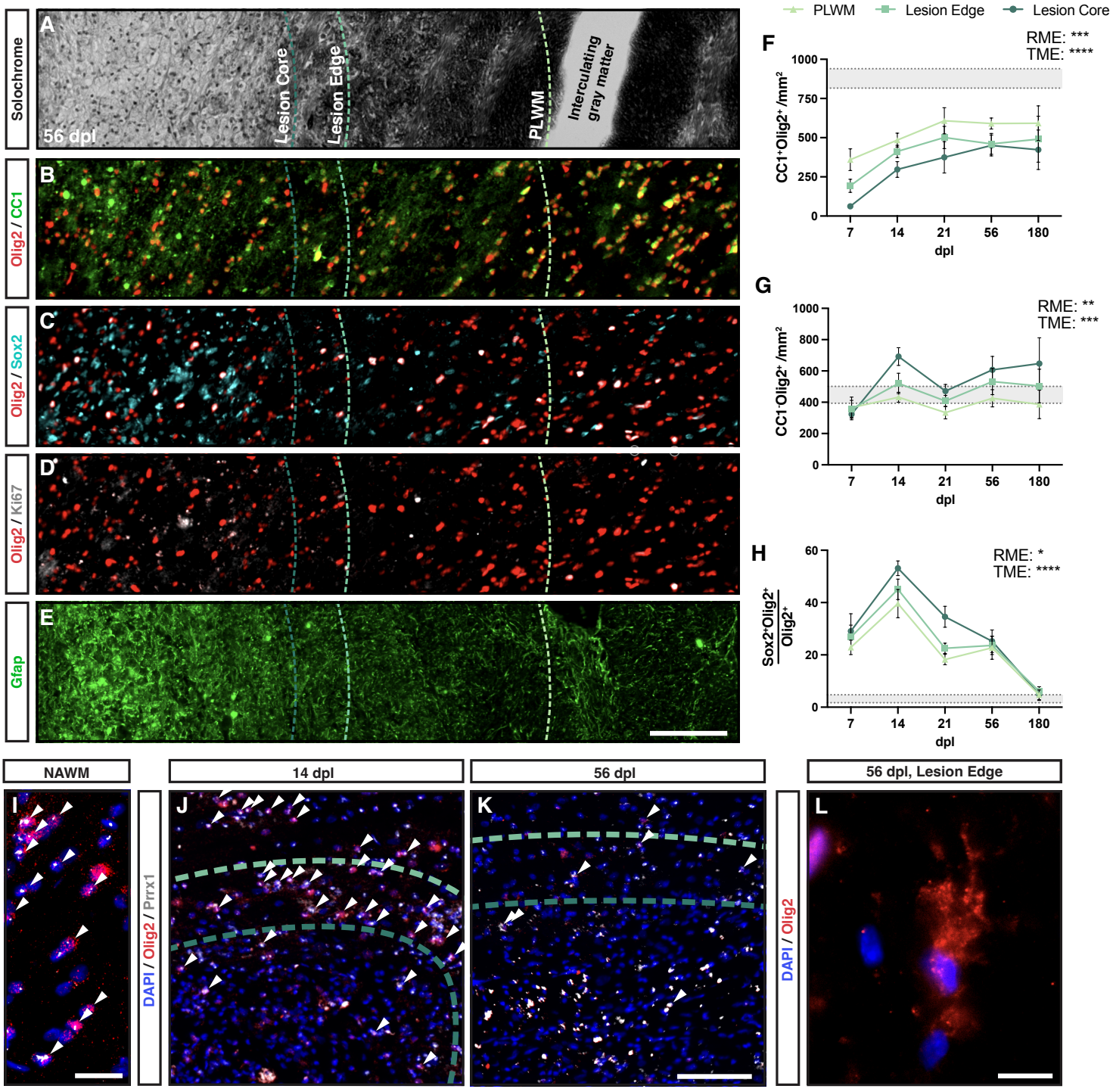

Figure 7

Scale Bar Figure 7A-F: 200µm

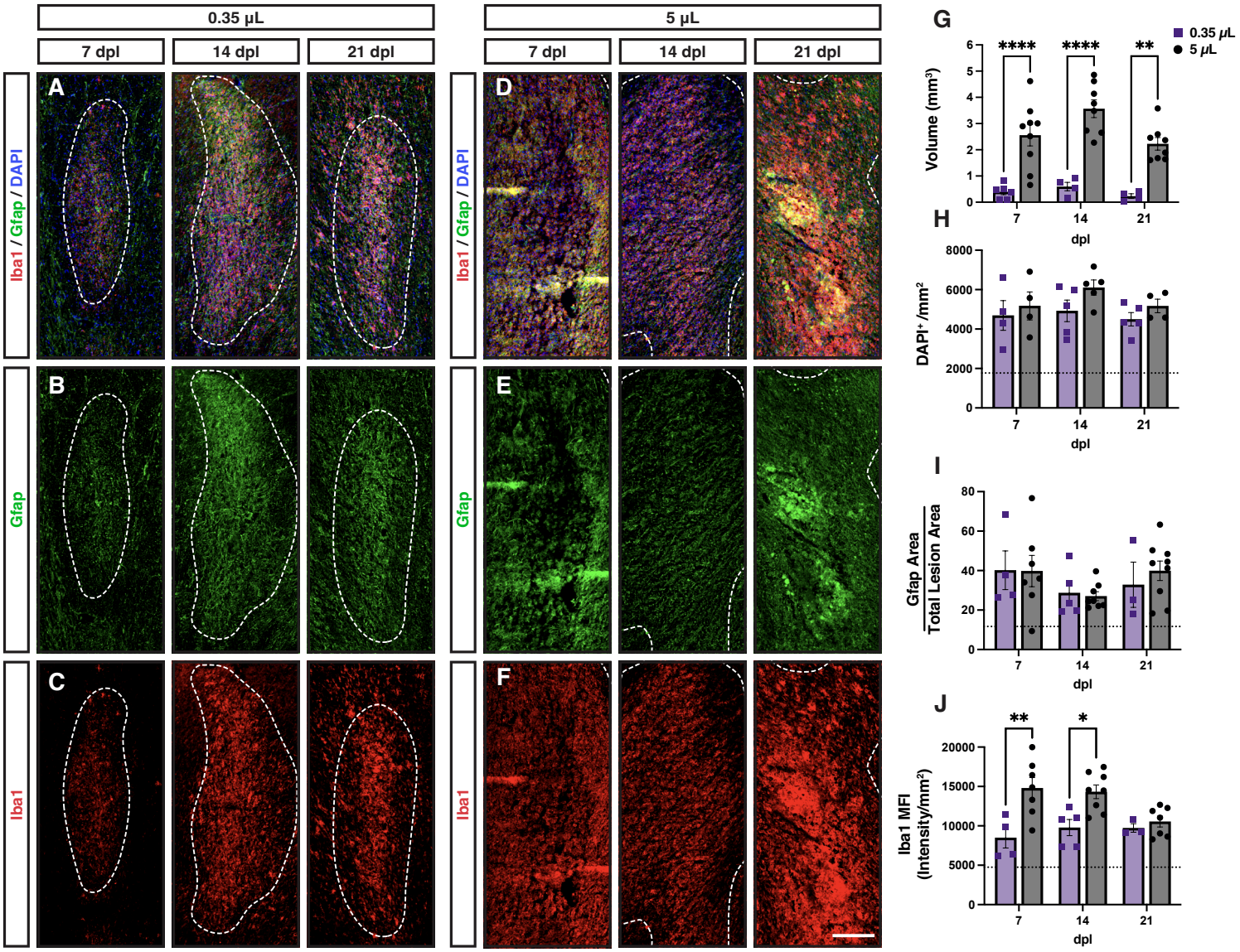

Figure 8
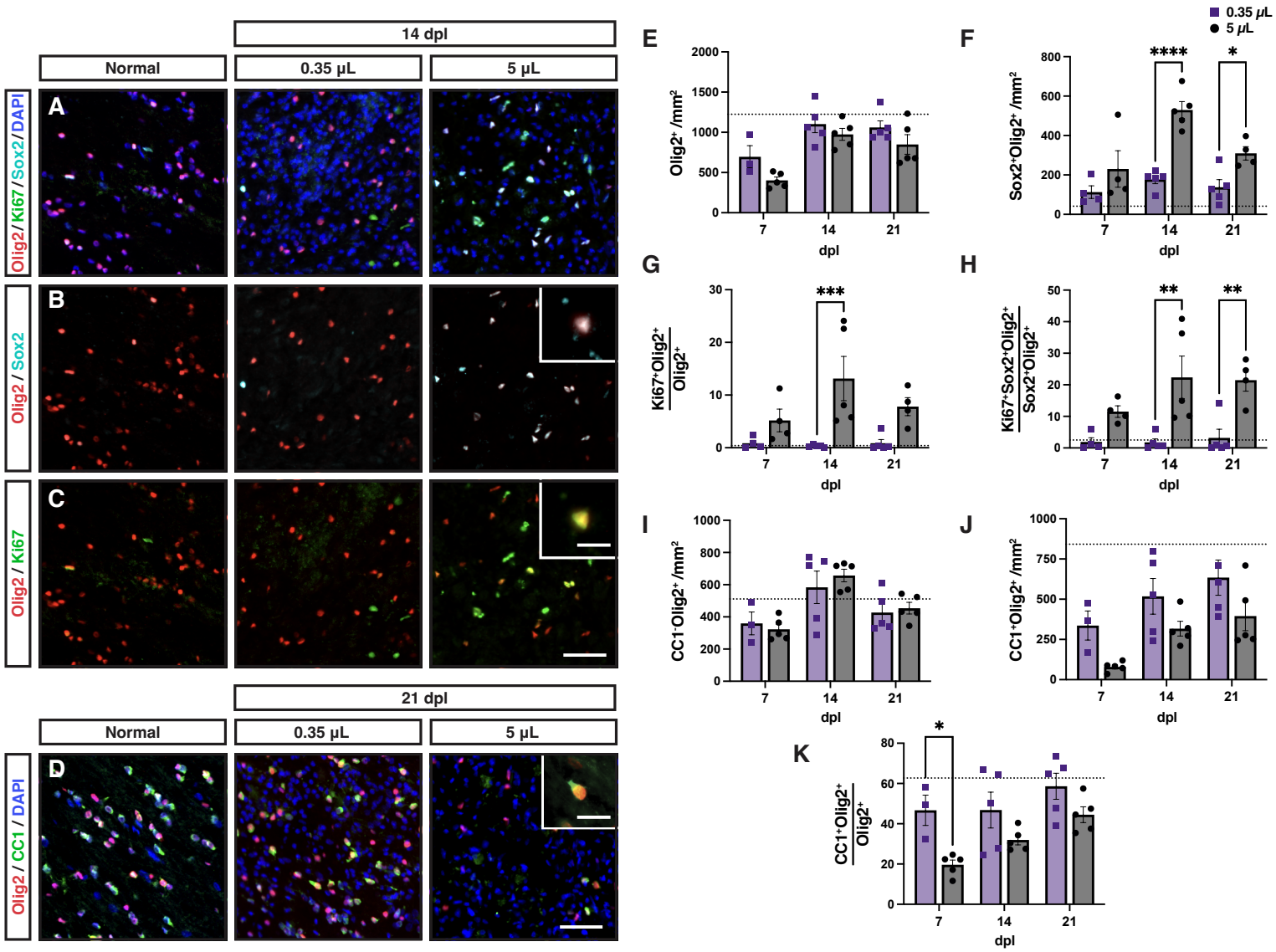
Scale Bar Figure 8A Inset: 10 µm
Scale Bar Figure 8 Whole Frame: 50 µm
Scale Bar Figure 8B-D Inset: 10 µm
Scale Bar Figure 8B-D Whole Frame: 50 µm